Electromagnetic Turbulence Control: Salt Water Experiments on an Axisymmetric Body

Promode R. Bandyopadhyay
John M. Castano
William H. Nedderman
Daniel P. Thivierge
NUWC Division Newport

Joseph Stupak

Albert R. Fredette
OASIS, Inc.

Naval Undersea Warfare Center Division
Newport, Rhode Island

20020205 101

PREFACE

Reviewed and Approved: 15 October 2001

Paul M. Dunn
Head, Torpedo Systems Technology Department

REPORT DOCUMENTATION PAGE

Form Approved
OMB No. 0704-0188

1. AGENCY USE ONLY *(Leave blank)*	2. REPORT DATE 15 October 2001	3. REPORT TYPE AND DATES COVERED

4. TITLE AND SUBTITLE

Electromagnetic Turbulence Control: Salt Water Experiments on an Axisymmetric Body

5. FUNDING NUMBERS

6. AUTHOR(S)

Promode R. Bandyopadhyay, John M. Castano, William H. Nedderman, Daniel P. Thivierge, Joseph Stupak, and Albert R. Fredette

7. PERFORMING ORGANIZATION NAME(S) AND ADDRESS(ES)

Naval Undersea Warfare Center Division
1176 Howell Street
Newport, RI 02841-1708

8. PERFORMING ORGANIZATION REPORT NUMBER

TR 11,317

9. SPONSORING/MONITORING AGENCY NAME(S) AND ADDRESS(ES)

Office of Naval Research
Ballston Centre Tower One
800 North Quincy Street
Arlington, VA 22217-5660

10. SPONSORING/MONITORING AGENCY REPORT NUMBER

11. SUPPLEMENTARY NOTES

12a. DISTRIBUTION/AVAILABILITY STATEMENT

Approved for public release; distribution is unlimited.

12b. DISTRIBUTION CODE

13. ABSTRACT (Maximum 200 words)

The control of turbulence in a turbulent boundary layer developing over a small axisymmetric cylindrical body in salt water at a moderate Reynolds number is considered in this report. Because near-wall turbulence production has a quasicyclic nature, an attempt is made to perturb the process by means of a periodic Lorenz force. A method of measuring the change in drag due to applied perturbations on a floating cylinder immersed in electrically charged salt water has been developed, and laser Doppler velocimetry measurements of changes in the near-wall mean velocity and turbulence have been carried out. Wall-pressure measurements have also been carried out to determine the effects of perturbation. The skewness and kurtosis of the wall-pressure fluctuation signal were found to increase slowly with the frequency of the Lorenz power pulsing to the microtiles. This pulsing leads to an amplification of wall-pressure spectrum power, which, although weak, provides support to the wall-layer resonance mechanism of the proposed microtiles.

14. SUBJECT TERMS

Lorenz Force	Turbulence Control	Wall-Pressure Fluctuations
Drag Reduction		

15. NUMBER OF PAGES
65

16. PRICE CODE

17. SECURITY CLASSIFICATION OF REPORT Unclassified	18. SECURITY CLASSIFICATION OF THIS PAGE Unclassified	19. SECURITY CLASSIFICATION OF ABSTRACT Unclassified	20. LIMITATION OF ABSTRACT SAR

NSN 7540-01-280-5500

Standard Form 298 (Rev. 2-89)
Prescribed by ANSI Std. Z39-18
298-102

TABLE OF CONTENTS

Section		Page

LIST OF ILLUSTRATIONS

Figure		Page

LIST OF TABLES

ELECTROMAGNETIC TURBULENCE CONTROL:
SALT WATER EXPERIMENTS ON AN AXISYMMETRIC BODY

1. INTRODUCTION

Over the last few decades, important progress has been made in the understanding of turbulence production in a turbulent boundary layer. It is now known that such processes are not entirely random. There are quasi-periodic mechanisms at play that are masked in noise. The discovery of this orderliness has opened up the possibility of a rational control of the turbulence production process and eventually of viscous drag and wall-pressure fluctuations. In 1832, Ritchie[1] demonstrated experimentally that a conducting liquid can be pumped when electric and magnetic fields are crossed within its bulk. Due to its high salinity content, seawater is reasonably electrically conducting. In principle, by crossing magnetic fields with electrical fields within a boundary layer, a Lorenz force can be produced to pump such a liquid locally. Additionally, the liquid's amplitude, phase, length, and time scales can be digitally varied. These developments open up the possibility of controlling the turbulence production process in an ocean-going vehicle.

Several years ago, the Naval Undersea Warfare Center (NUWC) Division Newport undertook research on this subject, although little was reported. Drag reduction experimentation remained elusive, although fluid pumping was demonstrated via flow visualization. Later, Princeton University researchers made claims of drag reduction that generated considerable interest.[2] These drag reductions were based primarily on local hot-film sensor response. Low-Reynolds-number transitional flat plate results were then scaled to high-Reynolds-number axisymmetric bodies; the mechanism was based on outer layer scaling. Flow visualization suggested the formation of large roller eddies. NUWC Division Newport efforts at reproducing these results were not successful.[3] In any case, the NUWC Division Newport and Princeton University efforts are noteworthy for their novel approach to a difficult problem.

1

The clearest evidence of drag reduction and turbulence suppression by the application of Lorenz force is derived from the low-Reynolds-number numerical channel flow simulation of Du and Karniadakis,[4] who kept the force distribution confined to the viscous sublayer. It was found that both transverse travelling waves and the spanwise oscillation led to drag reduction; the mechanisms which led to this finding, however, are not understood. Design of actuators that match the theoretical waveforms and the effects of Reynolds numbers are some of the issues that need to be overcome for an experimental reproduction of the numerical simulation.

Clear experimental evidence of whether the technique of electromagnetic drag reduction in salt water does indeed lead to a reduction of surface-integrated viscous drag is lacking. The Princeton University efforts are now focused on providing such evidence, as well as understanding the mechanism[5] by which it was obtained. A novel, single infinite tile is produced on one wall of a channel flow, with the other wall used as a reference. The edge effects are less than that in a flat plate boundary layer. Experimentation in a channel flow from outer layer to inner-layer-dominated marks a departure in Princeton University's approach to understanding the mechanism. Preston tubes and a pressure drop are used to compute drag reduction on the electromagnetic wall. A pressure drop can be used to accurately compute wall shear stress if the flow across the entire channel is fully developed and two-dimensional. It has been observed that a Preston tube registers a clear drop when the electromagnetic field is turned on.

1.1 BACKGROUND

During the planning stage, the present work has been influenced by past experience. Past Navy and NASA drag reduction efforts indicated that scaling from low to high Reynolds numbers and transitioning from laboratory curiosities to field tests can sometimes be problematic. Understanding of the non-linear turbulence mechanism tends to be a controversial and slow process. Techniques that work well in a turbulent flow, viz., polymer and microbubble injection, are probably not relevant because they involve large changes in fluid properties.

The general dimensions of the model and the experiment were arrived at as follows: Because past flat plate experiments on this method of control indicated a strong convergent-divergent edge effect,[6] the present experiment concentrated on an axisymmetric model. This eliminated at least one scaling issue and resulted in a better flow quality. Power consumption is bound to be an issue. Therefore, there is a need to resort to Lorenz forces that focused near the wall where turbulence production is at a maximum. As described in Bandyopadhyay and Castano,[7] the turbulence production statistical scales were first examined in large and small underwater bodies and in the NUWC Division Newport quiet-water tunnel based on wall-layer scaling. Fabrication limits then led to slightly higher dimensions. The wall layer scaling is an approximate guideline, and a mixed layer scaling effect is allowed in the boundary layer nature of the experiments.

There appears to be few general traits of drag reduction; however, there is one that is assumed to be relevant. The riblet work of Wilkinson and Lazos[8] showed that drag reduction is not uniquely related to the suppression of streamwise component of turbulence (u). Crawford and Karniadakis[9] have shown via the direct numerical simulation (DNS) of a low-Reynolds-number riblet channel flow that drag reduction is uniquely related to the suppression of the surface-normal component of turbulence (v) near the wall. The assumption is that this is a universal property of drag reduction. It is encouraging that an idealized, wall-normal Lorenz force modeling in a low-Reynolds-number turbulent channel flow indicates that a net drag reduction might be achievable because such an actuator requires less power compared to spanwise oscillation.[10] A structural modeling of a vortex in a unit flow domain has shown that vertical Lorenz pressure can lead to a suppression of wall-pressure root mean square (rms) levels.[11] It then follows that Lorenz pressure should be directed towards the suppression of the v-component of near-wall turbulence. This results nominally in an orthogonal array of magnets and electrodes. The reality, however, is far more complicated; the Lorenz pressure is only nominally surface normal in such an arrangement and it is, in fact, highly three-dimensional. A recent comparison of NUWC Division Newport's work with that of Kral[12] suggests that the induced flowfield of microtiles and macrotiles can be basically different. The attempt to control the v-component of turbulence rather than the u-component is hoped to further reduce the necessary Lorenz pressure levels. The present wall-layer-based arrangement of the magnets and

electrodes has been called microtiling here as opposed to the larger length scale based on the original Princeton University or NUWC Division Newport approach. In this manner, an attempt is made to greater understand the organized nature of turbulence production in a turbulent boundary layer.

The measurement problems in an electrically charged salt water medium are formidable. Because salt water is extremely corrosive, the longevity of electrodes and sensors is a problem. Many of the conventional diagnostics do not work easily. Because salt water is being electrically charged, ground looping can be a serious issue. Electrolysis can contaminate the response of hot films, and laser Doppler velocimetry (LDV) and particle image velocimetry (PIV) methods of diagnostics. Because the wall-shear distribution produced by each microtile is three-dimensional, the focus is on the surface and time-integrated viscous drag to clearly evaluate the drag reduction behavior. To be able to measure changes in drag due to the application of Lorenz forcing, the ratio of the tiled to the total surface area of the floating segment for drag measurement should be close to 1. Improvements have been made over past drag sensors and the longevity of the electrodes.

1.2 OUTLINE

This report is divided into three parts. First, the flow control mechanism is modeled. Here, a low-Reynolds-number experiment on a flat array of actuators and a complementary DNS simulation are discussed, and flow models are proposed. Secondly, the axisymmetric model experiment conducted at moderately high Reynolds numbers is presented; this experiment includes a description of the development of the drag measurement method. Third, the measurements for on and off conditions of Lorenz perturbation are discussed. The following measurements are reported: surface-integrated and time-averaged drag, near-wall LDV measurements of mean velocity and v-component of turbulence, and wall-pressure fluctuation (p_w) statistics. Measurements are also reported on a control cylinder containing only the electrodes (sans-magnets experiment). Measurements where higher order effects are observed are also discussed.

4

2. MODELING OF THE MECHANISM

The perturbation imposed by a single microtile actuator on the laminar and turbulent boundary layer flows is examined here. A closed-loop control would have the best payoff;[13] however, the quasi-cyclic nature of turbulence production might allow a simpler approach, namely the appropriate periodic forcing to affect the turbulence production process of the boundary layer without any regard for its phase. The spanwise oscillation of Jueng et al.[14] is such an approach. It should be noted that knowledge of the quasi-periodic instability process that leads to the production of turbulence in a wall-bounded flow is lacking; therefore, in general, an attempt is made to control the now familiar organized structures that are actually formed after the more important instability process has already occurred.[15]

2.1 LAYOUT OF THE SINGLE MICROTILE

Before building the axisymmetric model for the moderately-high-Reynolds-number experiment, it was deemed necessary to understand the potential effects of the microtile pulsing. A complementary low-Reynolds-number channel flow visualization experiment and DNS simulation were carried out, which are described in detail in Bandyopadhyay and Castano[7] and Hatay et al.[16] and are summarized below.

The statistical wall-layer turbulence production unit at a high-momentum thickness Reynolds number Re_θ of 22×10^3 was first studied. Here, $Re_\theta = U_\infty \theta / \upsilon$, where U_∞ is the freestream velocity, θ is the momentum thickness of the boundary layer, and υ is the viscosity of water. A scaled-down version of Re_θ to about 10×10^3 was then used as the starting design for a 5 x 5 array of a microtile that was fabricated on a flat printed circuit board. This is shown schematically in figure 1, where x and z are streamwise and spanwise distances, respectively. For example, if the field lines were straight and unaffected by the corners, the magnetic field

would run from the north to the south pole, while the electric field would run from the positive to the negative electrode. This would produce a nominally wallward Lorenz force that is oriented to null the *v*-component of wall turbulence. A finite-element computation was then carried out to determine the distribution of Lorenz force over the microtile. The fluid flow was neglected and was assumed to be uncoupled to the electromagnetic field. The maximum magnetic field was assumed to be 1 T and the applied electric potential was 1 V. The distribution is three-dimensional at the tile's center as shown in figure 2. This can be approximated as $k_1 \exp(-q_o d)$, where *d* is the lateral distance from the wall, and is negligible for $d > 2$ mm, $k_1 = 45$ (N/m^3), and q_o (1000/1.3) (m^{-1}).[13] The drop is exponential and the effective depth scales with the shortest scale of the microtile, which provides a guideline for keeping the field confined to the near-wall region.

Figure 3 shows a top view of the 5 x 5 array of the microtile. The design in figure 1 was modified and the electrodes were run continuously. Figure 4 shows the magnet assembly and measurements of the magnetic field. In a simplified simulation, the magnetic field is assumed to terminate on the surface;[16] however, the measurements show that the field lines are actually curved around the edges and penetrate below the surface.
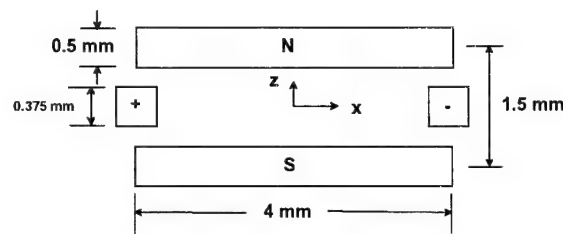
Figure 1. Top View of the Early Design of the Microtile
(Flow direction is along the x-axis and d is surface normal (see figure 2).)
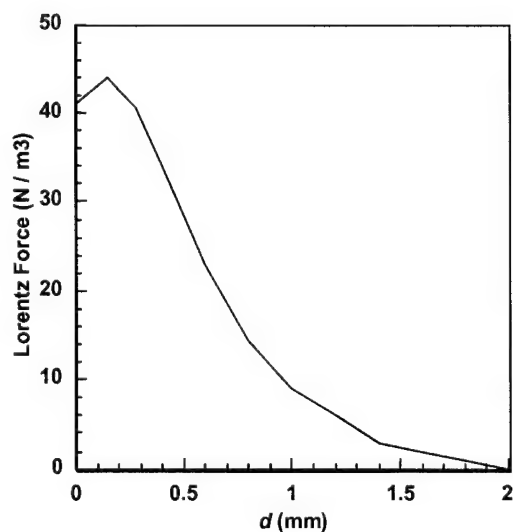
Figure 2. Computed Vertical Distribution of Lorenz Force in Stagnant Seawater at the Origin
of the Tile in Figure 1 (Maximum Magnetic Field 1 T and Electric Potential 1 V)
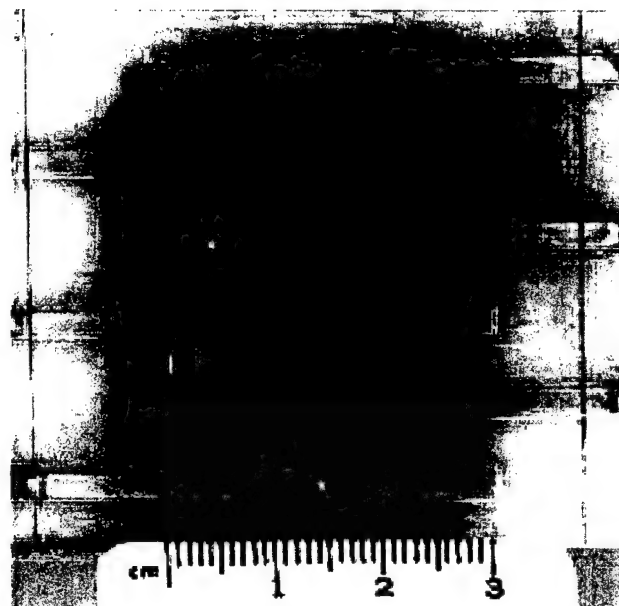
Figure 3. Top View of a 5 x 5 Array of Microtiles (The gold-plated electrodes run horizontally; the Ni-Fe poles run vertically in between.)
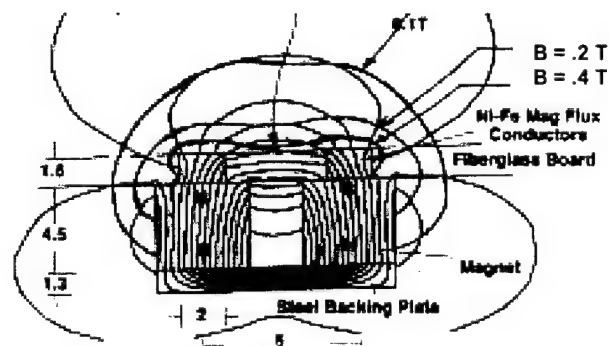
Figure 4. Approximate Plots of Magnetic Flux Density Amplitude (Thick Lines) and Flux Direction (Thin Lines) Versus Position (Dimensions are in mm.)

8

2.2 STOKES' LAYER MODEL

2.2.1 Laminar Perturbation Due to a Single Microtile

To understand the effect of pulsing the microtiles, a transitional channel flow visualization was carried out. The maximum Reynolds number was 557, based on channel depth (*2h*) and average bulk velocity. Salinity was 5% by weight. Dye was injected upstream through a series of wall-flush tubes aligned along the magnets and the tile centers. Both the visualization and computations indicated the flow to be stable without Lorenz pulsing. A 45% duty cycle, bipolar squarewave pulsing of electrode power was undertaken (figure 5). The dye was observed to form loops over the microtile array due to the imposed perturbations. There was no regeneration of turbulence downstream of the microtiles due to the stabilizing Reynolds number of the flow. Figure 6 shows the dye pattern. A model of the flow over the microtiles is shown in figure 7, where λ_y is the Stokes' viscous wavelength. This shows that pillows of vorticity have formed over each microtile, as if each was acting like an independent local wall oscillator. The result is that vorticity is diffusing out from the wall in a manner similar to Stokes' second problem. The formation of vorticity pillows modeled in figure 7 later received confirmation from the DNS simulation by Hatay et al.[16] The computed vorticity distributions over the microtiles are reproduced in figure 8. The distributions show that each pillow is actually composed of a pair of opposing signs of vorticity cells where the induced velocity is wallward in between. Note that these vorticity cell pairs or pillows have an opposite rotation to what occurs naturally in a turbulent boundary layer near the wall.
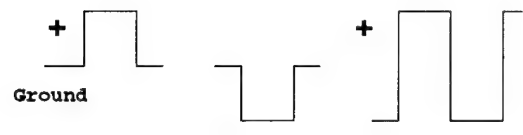
***Figure 5. Voltage Waveforms of Power to Electrodes: Positive Unipolar,
Negative Unipolar, and Bipolar***
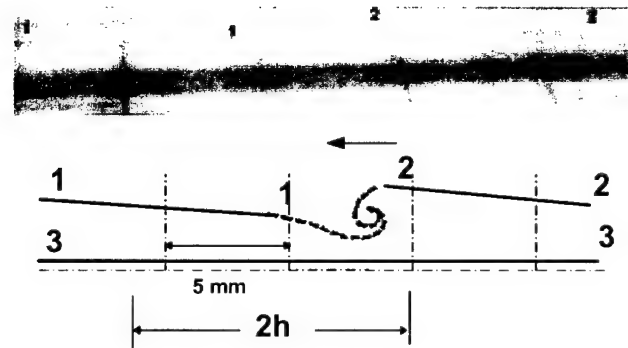
***Figure 6. Downstream Dye Pattern with Pulsed Lorenz Force (Side view: (a) video print, (b)
schematic of (a). Chain lines are 5-mm x 5-mm grid patterns. Re = 400.
Bulk flow speed 31.2 mm/s. Channel height is 2h (11.5 mm).)***
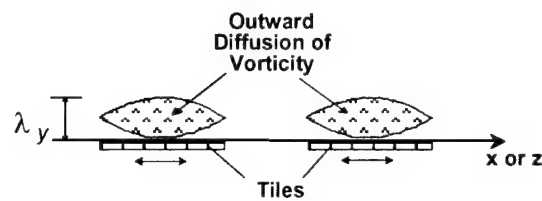
Figure 7. Stokes' Layer Analogy of Pulsed Lorenz Force

10
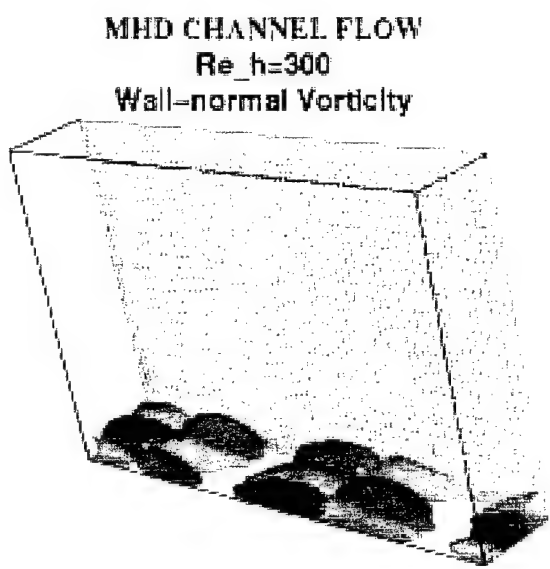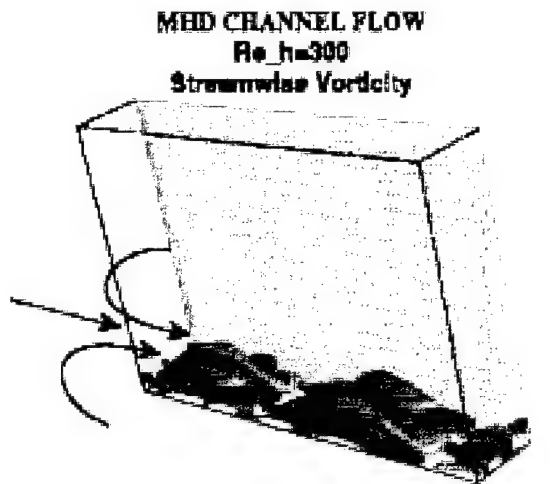
Figure 8. DNS Simulation of Streamwise Vorticity Perturbation Induced by the Microtiles, after Hatay et al. (The induced flow between the streamwise vorticity pairs is wallward.)

This Stokes' layer resonance model of vorticity accumulation over the microtiles proposed by Bandyopadhyay and Castano[7] was later generalized by Meng.[17] Assume that pulsed Lorenz pressure is analogues to oscillating a wall that gives rise to a Stokes' layer of vorticity perturbation. Also assume that the quasi-viscous near-wall region of a turbulent boundary layer could behave like a Stokes' layer when pulsed. It is known that turbulence production peaks at

$$10 \leq \frac{yU_\tau}{\upsilon} \leq 15 . \tag{1}$$

Here, y is surface-normal distance, U_τ is friction velocity, and υ is fluid viscosity. When Stokes' layer viscous wavelength matches the depth for maximum turbulence production, some interference can be expected. This condition is given by

$$\frac{10\upsilon}{U_\tau} \leq \sqrt{\frac{2\upsilon}{\varpi}} \leq \frac{15\upsilon}{U_\tau} . \tag{2}$$

If $\varpi = 2\pi f_B$, where f_B is the pulsing frequency, then

$$314 \leq \frac{(U_\tau)^2}{f_B\upsilon} \leq 707 . \tag{3}$$

Note that due to equation (1), condition (3) is calibrated against turbulence production structure statistics. At a freestream speed of 8 m/s, in the middle of the floating cylindrical section of the model (figure 9) where the boundary layer is turbulent, $U_\tau = 0.33$ m/s and $\upsilon = 11.4 \times 10^{-7}$ m^2/s, the pulsing frequency should then be

$$135\,\text{Hz} \leq f_B \leq 304\,\text{Hz} . \tag{4}$$

It should be noted the length and time scales have been examined for the above calculations. However, an examination of the required amplitudes of perturbation, namely the amount of fluid pumping to be undertaken by the actuator, was not undertaken.

3-Inch Diameter EMTC Model in NUWC Salt Water Tunnel
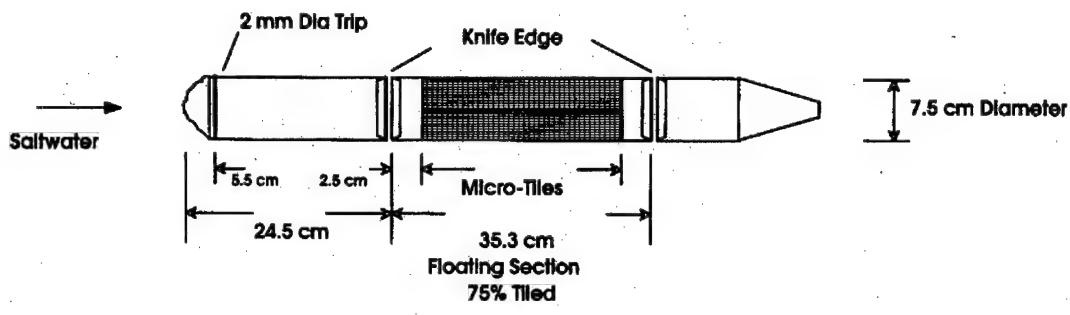
$Re_x = 1.13 \times 10^6$ at
Freestream Speed of 5.3 m/s
at Left Side of Knife's Edge
(Schlichting[18])

At 5.3 m/s, Estimated Values are
$c_f = 0.0035$ $Re_\theta = 2300$ $U_\tau = 0.2$ m/s
$\sigma = 4$ mho/m, $V_o = \pm 10$ V, $B_o = 0.6$ T
$\rho = 1000$ kg/m³ $N_\tau = \pm (\sigma V_o B_o)/(\rho U_\tau^2) = 0.6$

Figure 9. Schematic of the Model and the Experiment

2.2.2   Turbulent Flow Mechanism of a Single Microtile

The main control experiments were carried out on a 76-mm-diameter axisymmetric cylinder, which is described in the next section and shown in figures 9 and 10. This cylinder had a floating section for measurement of drag changes. This section contained numerous microtiles (figures 9 and 11). In the early stages, the measurements of boundary layer integral quantities over a similar model proposed by Castano[19] were adopted to determine the volume of influence over one microtile in wall-layer coordinates (figure 12). Note that the volume is roughly the same as one unit domain of turbulence production at a freestream speed of 5 m/s. It can accommodate one near-wall vortex pair and the location of maximum turbulence production. The depth also covers the region of overlap between the outer and inner layer.
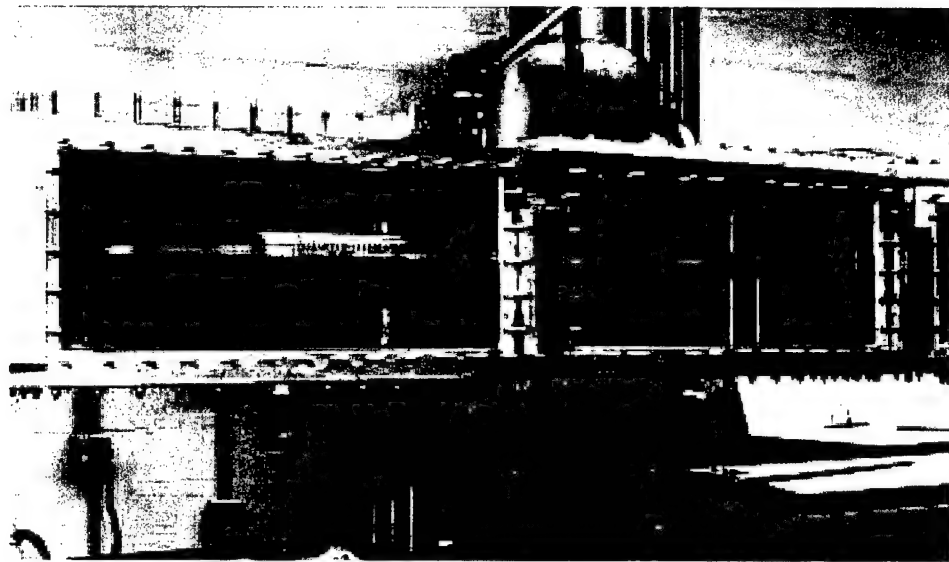
Figure 10. Photograph of the 75-mm, 3-in.-Diameter, 1-m-Long Model in the Water Tunnel (The electromagnetic floating section is visible in the middle.)
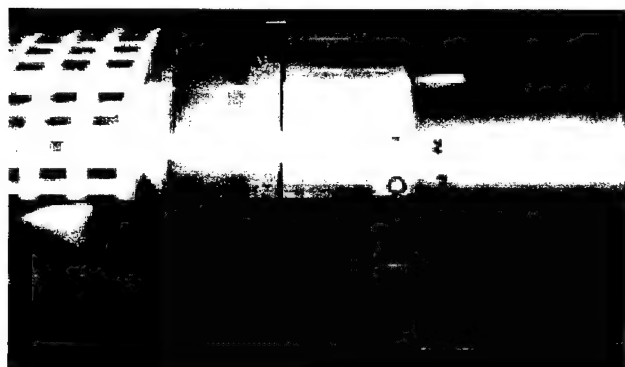
Figure 11. Photograph of Wall-Pressure Sensors (Cylinder nose is on the left. The horizontal ruler shows the alignment of sensor 1 with the middle of the upstream microtile and in between the magnet pairs. The black rectangles are magnets and the vertical shining bands are the electrodes. The knife edge is in the middle of the photograph. Flow is from left to right.)
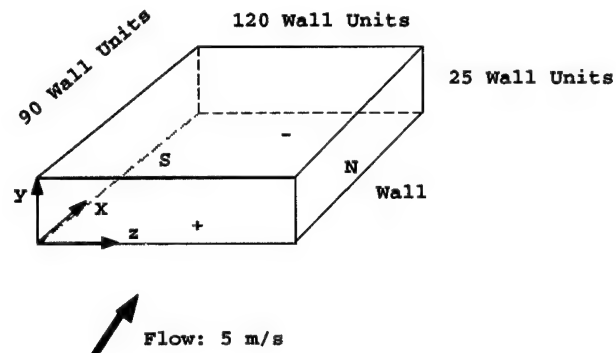
***Figure 12. Volume over One Microtile in Wall Units at 5 m/s
Where Lorenz Force Field is Being Applied***

A model can now be developed for a turbulent boundary layer suddenly encountering a surface populated with many microtiles (figure 13). Recall that Lorenz pulsing gives rise to pillows of alternating vorticity that have an opposite rotation to what naturally occurs in a turbulent boundary layer unit production domain. The qualitative nature of the vorticity distribution due to the microtile pulsing shown in figure 8 is generally valid. It remains the same in quiescent, laminar, and low-Reynolds-number turbulent flows and with several different kinds of pulsing.[16, 20] At a freestream speed of 5 m/s, the spanwise scale of the normal and microtile-perturbed vorticity pairs will match (figure 13). Therefore, it is proposed that the microtiled turbulent boundary layer provides a layer of vorticity pillows whose sense of rotation is opposite to what normally occurs in a turbulent boundary layer. It remains to be seen whether this translates to any near-wall vorticity cancellation or drag reduction. It should be noted that the DNS simulation is for a low-Reynolds-number channel flow, and its vorticity pillows are assumed to be valid at the moderately high Reynolds number of the present experiment on turbulent boundary layers.

EMTC Microtile Drag Reduction Mechanism
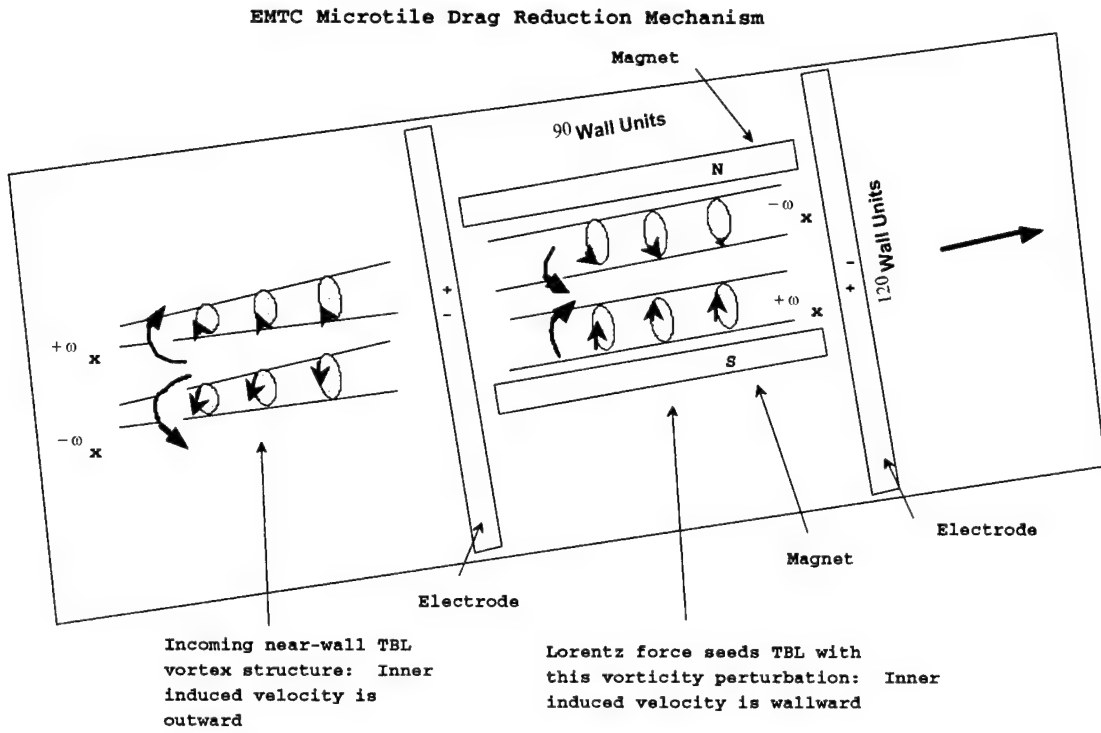
Figure 13. Conceptual Sketch Showing How an Incoming Regular Near-Wall Vortex Pair in a Turbulent Boundary Layer Will Encounter an Opposing Pair Near Wall over a Microtile

2.3   PULSED MICROTILES AS SPANWISE WALL OSCILLATION ACTUATORS

As shown above, the pulsed microtiles create a thin layer (or barrier) of pillows of vorticity between the wall and the incoming boundary layer. If effective, this mechanism should inhibit turbulence production. This approach is similar to that of Jueng et al.,[14] which also inhibits the interaction of the boundary layer with the wall by means of spanwise wall oscillation. Because this approach, while still in the realm of academic curiosity, is well validated via low-Reynolds-number DNS simulation and laboratory experiments, it is instructive to examine the present actuator in its framework. This addresses the valuable question: What kind of electromagnetic microtile actuator would replicate the required spanwise wall motion proposed by Jueng et al.?[14]

Assume that pulsing of the electromagnetic microtiles is analogous to the spanwise wall or fluid oscillation proposed by Jueng et al. and Choi et al.[21] A summary of their low-Reynolds-number drag reduction results appears in figure 14 of Choi et al.[21]

Propose that near-wall vorticity breakdown will be interrupted if spanwise wall or spanwise fluid displacement follows the relationship in equation (5), where the spanwise magnet spacing b is as shown in figure 14:

$$b^+ \geq 100, \tag{5}$$

where $b^+ = \dfrac{bU_\tau}{\upsilon}$. From figure 14 of Choi et al., the Strouhal number for maximum drag reduction due to turbulence suppression (50%) is given by

$$10 \leq \frac{\Delta z \varpi}{2U_\tau} \leq 15, \tag{6}$$

$$10 \leq \frac{b 2\pi f_b}{2U_\tau} \leq 15, \text{ and} \tag{7}$$

$$3.2 \leq St_b \leq 4.8 . \tag{8}$$

Here, St_b is a Strouhal number and f_b is the pulsing frequency. Note that turbulence reproduction physics, namely viscosity and information about structure organization, are already accounted for in equation (8). In the middle of the current 76-mm-diameter model floating section where $U_\tau = 0.33$ m/s, the pulsing frequency is

$$210\,\text{Hz} \leq f_b \leq 315\,\text{Hz} . \tag{9}$$
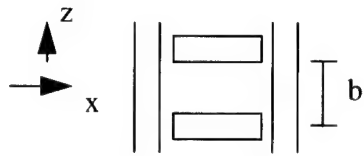
Figure 14. Sketch of a Microtile (Dimension b is the width of the microtiles.)

It is interesting to see that the range of f_b in equation (9) is practically the same as that of f_B in equation (4). This suggests that the original Stokes' layer resonance hypothesis given earlier incorporates the same physics as that of the large drag reduction due to spanwise wall oscillation. With the correct length and time scales, the present microtile should then be able to generate a spanwise fluid oscillation given by equation (8) for a drag reduction of 50% to occur, if the $j \times B$ field amplitude is able to pump the salt water to the extent required.[22] Here, j is the current density in A/m^2 and B is the magnetic induction in T. The focus then is on the question of whether the actuator is able to physically move the near-wall fluid spanwise per cycle over the required distance.

3. EXPERIMENTS AND UNCERTAINTIES

The axisymmetric model experiments have been carried out in the NUWC Division Newport stainless-steel salt water tunnel, which is a closed-circuit tunnel with variable pressure capability. The test cross section is 30 cm x 30 cm and 3 m in length. Separate computers have been used to control the drag balance, the pulsing of power to the microtiles, and the laser Doppler velocimetry system. A main computer has been used to monitor the tunnel properties and acquire, process, and display all the flow data from the other computers in a central file.

The 5 x 5 array microtiles developed on a printed circuit board have been used as the model for building an axisymmetric model sketched in figure 9. Figure 10 shows the model in the NUWC Division Newport stainless-steel salt water tunnel. The floating section is microtiled. The front and back parts of the model rest rigidly on a hollow stainless-steel rod through which all coiled wires pass. The electrodes are placed in a cross-stream direction while the three-dimensional permanent magnets (1280) are aligned axially. All microtiles are pulsed in phase. At a speed of 5.5 m/s, the interaction parameter defined as the ratio of applied Lorenz force times viscous force divided by the square of inertia force, $N = \frac{\sigma V_o B_o}{\rho U_\tau^2}$ is 0.6. Here, σ is the electrical conductivity of the fluid, V is the scalar electric potential, B is magnetic flux, ρ is fluid density, U_τ is friction velocity, and the subscript o denotes conditions at the wall.

3.1 QUALITY OF SURFACE SMOOTHNESS

In the water tunnel, the model is mounted on a sting attached to a cruciform. Due to sting mounting, at high tunnel speeds (7 m/s) the model nose vibrates, the reason for which is unknown. The test cross section is 30 cm x 30 cm, which causes an area blockage of 5%. The boundary layer was tripped with a 2-mm diameter O-ring sealing. These trips do not last long in salt water. The estimated boundary layer integral quantities over the floating section at 5 m/s are given in figure 9. Although not visible to the naked eye, the seemingly filtered water contains

fine particles of rust, which are smooth to the touch. It is possible that this rust roughness has a moving surface and is not akin to a solid sand grain roughness. In the course of about 1 hour, these rust particles accumulate over the magnets in the shape of a ramp. Figure 15 shows an impression of the rust deposition. The rust deposit should bring the Lorenz force slightly into the boundary layer. Care was taken to minimize the rust deposition by means of filtering. In the present work, the magnets lie below a thin kapton layer on which the electrodes are electroplated. Over time, these electrodes may form microscopic cracks but do not form a gouging or roughness. In the present work, rust is the only source of roughness, which can be minimized after intensive filtering. On the other hand, in many other experiments where tile fabrication did not follow the electronic fabrication procedure as here, the plates may be far from being hydrodynamically smooth due to corrosion.

Figure 15. Impression of Accumulation of Rust Roughness over the Magnets (Top ruler numerals are in inches and the bottom are in cm. The dark areas below the ruler are from the rust deposition. The flow is from left to right, with the rust forming a ramp to the flow.)

3.2 DRAG BALANCE

In early experiments on the axisymmetric model, an in-house-built drag sensor was used. Later, this was replaced by a commercial balance (ATI, Inc.), which was further developed for salt water application. The balance stiction problem, which prevents the floatation in the floating section, was eliminated by using four parallel flexures to stiffen and support the floating cylinder. Internal cables were coiled, and the in-house sensor was replaced by an ATI, Inc. nano sensor, a six-component balance of integral construction. The gain has temperature compensation but the intercept does not. The sensor and the cables were coated for electrical insulation and use in salt water. The sensor was installed in the model and dipped for days in a salt water bath (30 mSi/m, 16.9 gm/l of salt at 18°C). The model was stiff and showed no visible movement when drag loads were applied. The calibration was linear in both air and salt water over periods of hours, during which the electrodes were powered on and off. Figure 16 shows the long timetrace of the sensor output for 5 V and 10 V, 70 Hz, positive and negative unipolar and bipolar pulsing of electrode power (figure 9) under zero axial loading, and a loading of 100 g/ms. There is a maximum uncertainty of 5 g/ms at 10 V and 26 A total bipolar pulsing in the no-load case. When there is a loading of 100 g/ms, bipolar pulsing may appear as a 5% drag reduction after 15 minutes of powering. These are the minimum levels of uncertainty achieved and seem acceptable.
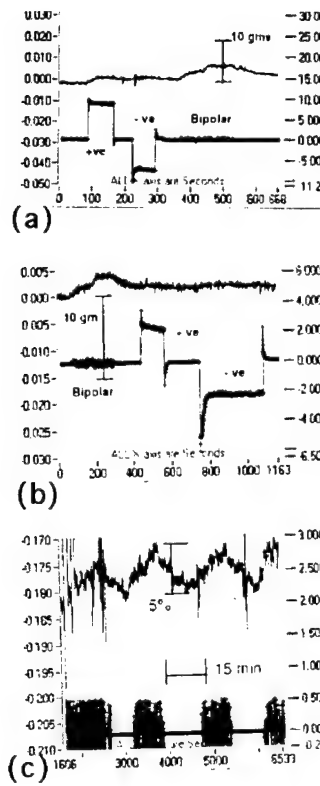
***Figure 16. Time Trace Showing Uncertainty in Response to ATI Nano-Coated Sensor
(Left axis: drag; right: electric field. (a) no weight drag, 10 V; (b) no weight drag, 5 V; (c)
100-gm weight axial force, 10-V bipolar pulsing. Salt water bath: 30 – 31 mSi/m,
17 – 18 gm/l of salt at 18 – 19°C. Model is in an aquarium.)***

3.3 ELECTRODE PULSING

The present experiments were carried out with three kinds of pulse shapes shown in
figure 5: unipolar positive, unipolar negative, and bipolar. The voltage level is close to 3 V to
minimize electrolysis. The electrodes were made of pure copper, and nickel and gold plating
were applied to reduce corrosion. The electrodes were electroplated on kapton layers, where the
surface discontinuities were of electronic industry resolution rather than of mechanical or
electrical engineering resolution. This fineness of surface finish, plus the choice of frequencies
and pulse shapes, helped to minimize or eliminate electrolysis. The magnets remained under the
kapton layer and were not exposed to salt water. The bus bars inside the cylinder were insulated.

22

The control circuit was software programmed to vary the pulse form and frequency. The applied voltage varied between ± 10 V, 0 to 10 V, 0 to -10 V, 0 to 5 V, or 0 to -5 V. The current level over the entire floating section was a maximum of 24 A. Measurements in flat plates in a salt water aquarium in the NUWC Division Newport laboratory indicated that heating of water does not bring a sufficient change in viscosity to cause a drag reduction. Electrolysis is also not a source of drag reduction or possible noise. The model and the ATI sensors were dipped in an aquarium of salt water for several days. The calibration was checked with electrode power turned on and off. A floating cylinder was also fabricated with magnets and not the electrodes.

3.4 SANS-MAGNETS EXPERIMENT

A question was raised whether thermal heating due to the electrodes contributes to a drag reduction or a gauge response that is similar. Figure 17 shows schematically the thermal plumes that can trap recirculating bubbles and then generate a thrust. A new model was constructed with the electrodes present but without the magnets. Both the NUWC-Division-Newport-made strain gauge balance and the ATI commercial balance were used. No change in drag was observed without the magnets.

Measurements of wall pressure spectra were carried out in the sans-magnets case and are shown in figure 18. The wall-pressure sensor, located at the downstream end of the floating section, contains the rows of electrodes (figure 11). It is interesting to see that, in an average of 20 spectra, a 2.4-dB reduction is observed at 75 Hz, the frequency of pulsation. There is no significant reduction over the entire frequency range; however, it is intriguing to see that even at such a reasonably high-Reynolds-number turbulent boundary layer, a spanwise array pulsation could be picked up downstream, albeit in a narrow-frequency range, and only near the frequency of pulsation. The waveguide nature of the viscous sublayer might have helped make this localized organization possible.

Water BL

Smooth Flat Plate /
Axisymmetric Body

Thermal Plumes

Heating Elements

$-c_f$

Thermal Plumes

Recirculation Zone: TBL Riding
Over, Reducing Turbulence Production

Heating Elements:
Pulsed to Reduce
Electrolysis

March 31, 1997
Bandyopadhyay
NUWC

No magnets causing roughness accumulation
Simpler skin
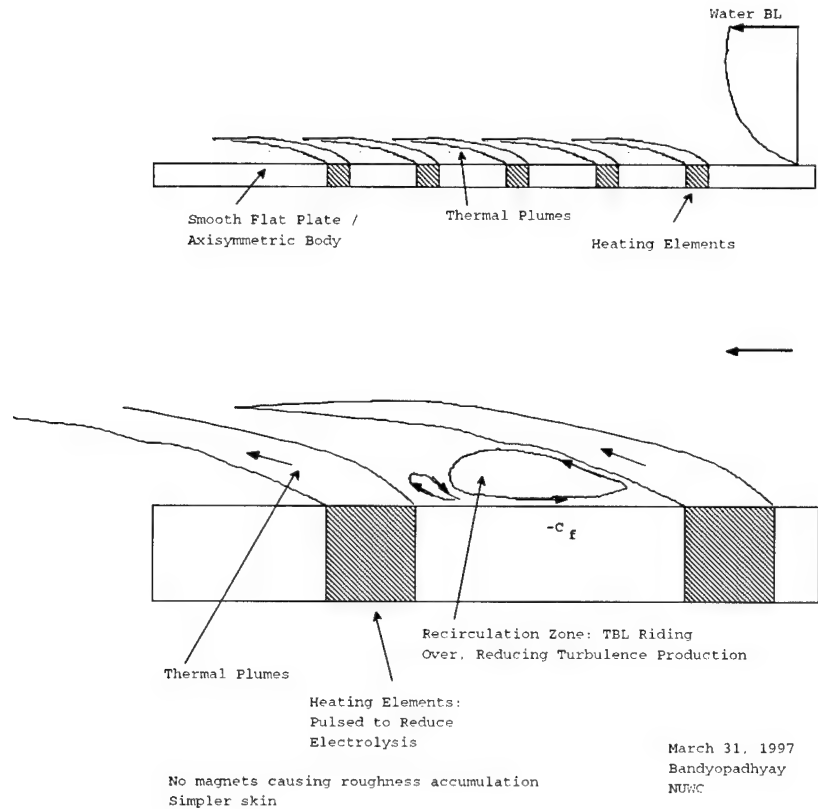
Figure 17. Conceptual Basis for the Sans-Magnets Experiment (Schematic representation of possible drag reduction arising from recirculating bubbles fostered by thermal plumes from the electrodes.)

24
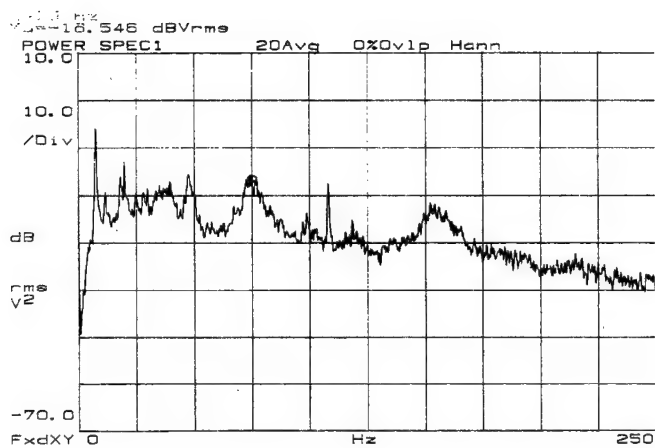
Figure 18a. Wall-Pressure Spectrum Downstream of the Electrodes in the Sans-Magnets Experiment (Freestream speed is 17.3 ft/sec and electrode power is off.)
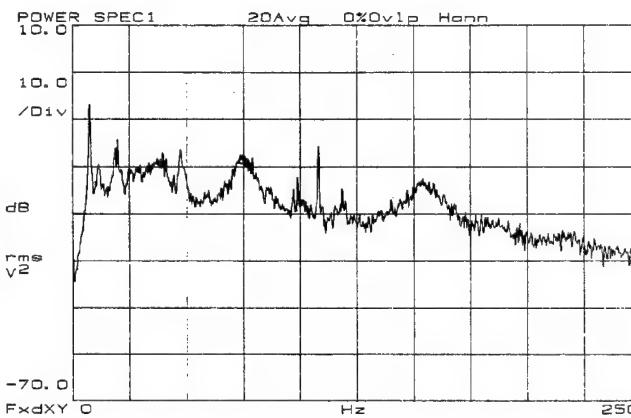
Figure 18b. Wall-Pressure Spectrum Downstream of the Electrodes in the Sans-Magnets Experiment (Freestream speed is 17.3 ft/sec and electrode power is on at ± 8 V, ± 20 A pulsed bipolar at 75 Hz (note a reduction of 2.4 dB at 75 Hz.).)

25

3.5   LASER DOPPLER ANEMOMETRY

3.5.1   Instrumentation

The instrumentation employed to measure the two-component velocity profiles consisted of a standard TSI laser Doppler anemometry (LDA) 9100-7 system with support software interfaced to a computer for data management and reduction. An Argon-Ion 10-W Coherent laser illuminated the sampling volume through which 1.5-micron (normal-size distribution) silicon-carbide particles passed, reflecting blue-green light for the backscatter optics configuration to observe. The reflected light or burst signal was analyzed by a TSI counter-type 1980B signal processor with a MI-990 multichannel interface. The TSI interface/software package (called FIND) allowed for simultaneous two-component measurements with up to 8,000 single realizations per data point of velocity. Table 1 details the dimensional values of the sample volume (ellipsoidal in shape) generated by the optical configuration employed.

Table 1. Sample Volume Dimensions

d_m	l_m	d_{fr}	N_{fr}
100 μm	1908 μm	4.91 μm	20.3
d_m = diameter of LDA sampling volume l_m = spanwise length of LDA sampling volume d_{fr} = individual fringe width N_{fr} = number of fringes in sample volume			

The TSI 9400 traversing mechanism achieved a repeatable positioning accuracy of ± 0.05 mm in all three spatial planes. Velocity bias corrections were applied. The LDA signal processor operated in the total burst mode.

26

3.5.2   Laser Doppler Calibration Procedure

Slight changes in optical alignment (i.e., the half-angle of the intersecting beams), due to temperature gradients in the equipment or other distortions caused by traversing through windows, can alter the fringe spacing significantly. This is particularly true when the half-angle is small, for example, 3°, so that a ± 0.3° angle error could result in a 10% velocity measurement error. This fringe distortion can cause errors in absolute velocity measurements (i.e., when the laser data are used to calibrate other flow instrumentation) and are most noticeable over large traverse sweeps. To correct for this distortion error, a shutter wheel device was placed at the profile locations of interest and LDA calibration sweep measurements were made. Slight deviations in the optical beam half-angle can then be corrected until the LDA-measured velocity agrees with wheel rpm information monitored on an oscilloscope. The wheel has a radial and concentric line pattern on a transparent film wheel surface that allows precise positioning of the sample volume. An added feature when using the wheel calibration technique is the ability to measure trial profiles along the wheel in any quadrant, thereby confirming the frequency shifts to use for the desired measurements. For the measurements described here, both beams were shifted up to 500 kHz, with a low- and high-bandwidth filter of 100 kHz and 1 MHz, respectively. Finally, the beams were slightly tilted down horizontally (approximately 0.5°) so that the sample volume hits the surface before the beams are clipped by the flat plate structure themselves.

3.5.3   Procedure During Data Acquisition

The test procedure consisted of positioning the sampling volume at the desired streamwise location and lowering it until the X-pattern made by the u-component horizontal intersecting beams symmetrically straddle the surface. This provides a position error of ± 50 μm (or roughly half the sample volume diameter) in the vertical y-axis and streamwise x-axis, with an error of ± 0.5 mm in the spanwise z-axis (due to the sample volume's shape). Measurements were made near the centerline of the test section, where spanwise flow deviations were considered minimal. Once the zero height position was selected, the automated data

acquisition system would be activated, allowing the traverse to begin taking data at the predetermined test points. A time-acquisition limit of 3 minutes per data point was established to avoid waiting for a non-existent signal where no seed was present in the flow. This allowed for the vertical v-velocity component signals to kick in once their beams had cleared the surface of the plate. The vertical profiles consisted of 20 to 30 data points, each consisting of approximately 8000 single realizations or velocity measurements. At the end of each sweep, a statistical analysis of the profile was carried out and a preliminary plot of the profile was produced to validate the measurement. After the data were catalogued and stored, the traverse was asked to return to its starting point and the error in the zero position was measured. The LDA beam's zero point was then reset, the current flux desired applied, the freestream velocity set, and another profile sweep initiated. Any other important fluid variable, i.e., fluid temperature and static pressure in the test section, were recorded separately during each test run.

4. RESULTS AND DISCUSSION

The measurements of drag, mean velocity, turbulence, and wall pressure in the 76-mm-diameter model for Lorenz force on and off cases are discussed below.

4.1 MEASUREMENTS OF DRAG, MEAN VELOCITY, AND TURBULENCE

The baseline measurements for no power to the electrodes (the Lorenz-force-off case) are shown in figures 19 – 22. The measurements of baseline drag on the floating cylinder versus freestream speed for no-electrode power are shown in figure 19. The distribution follows a power law where the exponent 1.89 is close to the expected square law trend. The drag balance seems to be reliable and the effect of roughness does not appear to be strong. The data are also compared to a trend line for a mean skin friction coefficient of 0.0028. The laser Doppler measurements of the mean velocity profile are shown in figure 20. They are compared with a smooth and a rough wall log law. Here, $U^+ (= U/U_\tau)$ and $y^+ (= yU_\tau/\upsilon)$ are streamwise velocities and surface normal distances in wall-layer variables, U_τ is friction velocity, and υ is the kinematic viscosity of the salt water. The effect of roughness does not appear to be strong. The laser Doppler measurements of streamwise turbulence intensity are shown in figure 21. Here, u_{rms} is the rms of fluctuations of streamwise velocity and δ is the thickness of the turbulent boundary layer. The measurements fall on the upper bound of the published smooth-wall data. The measurements of the surface-normal component of turbulence intensity are shown in figure 22. Here, v_{rms} is the rms of fluctuations of surface-normal velocity. The measurements are close to published data for smooth walls. The drag balance and laser Doppler measurements are acceptable and are akin to those for smooth walls.
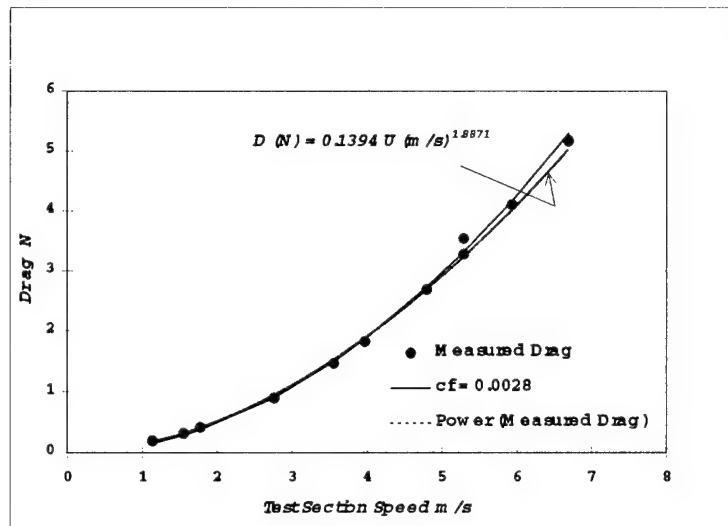
Figure 19. Validation of Drag Balance (Power-Off Case)
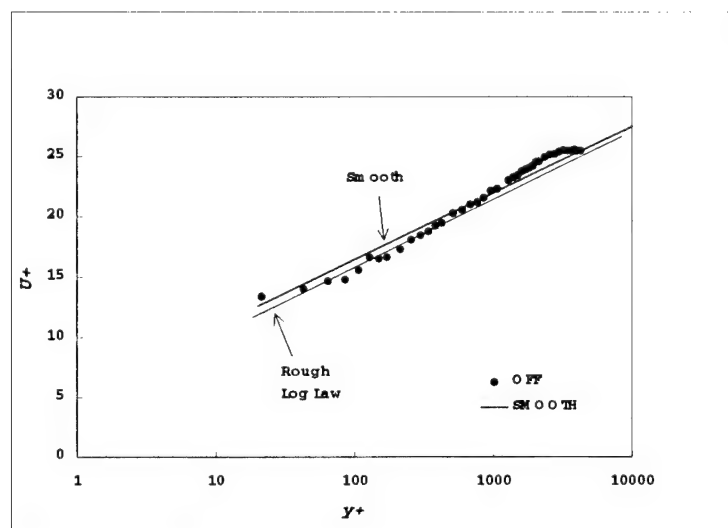
Figure 20. Laser Doppler Measurements of Baseline Mean Velocity Profile at the Downstream End of the Floating Section Compared with Smooth Wall Profile

30
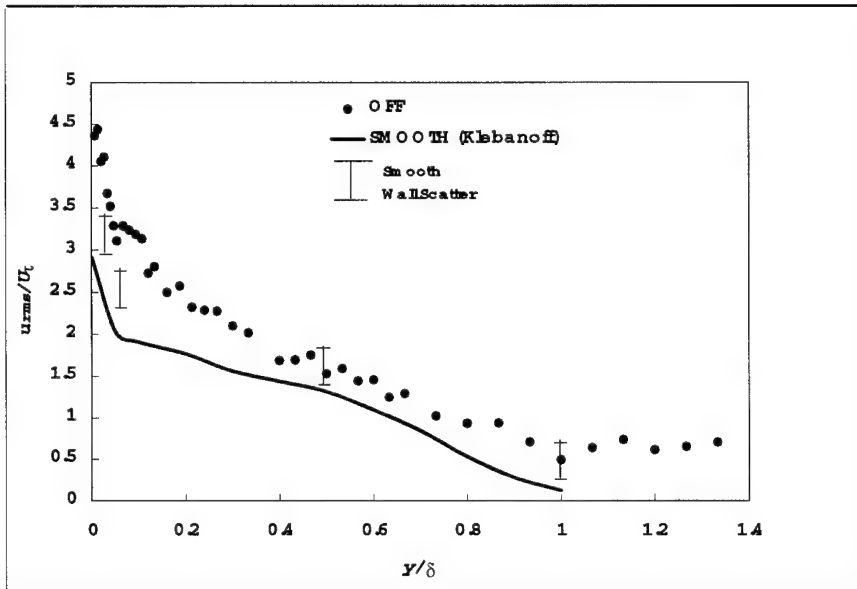
Figure 21. Laser Doppler Measurements of Baseline Streamwise Turbulence Profile at the Downstream End of the Floating Section Compared with Klebanoff's Smooth Wall Profile
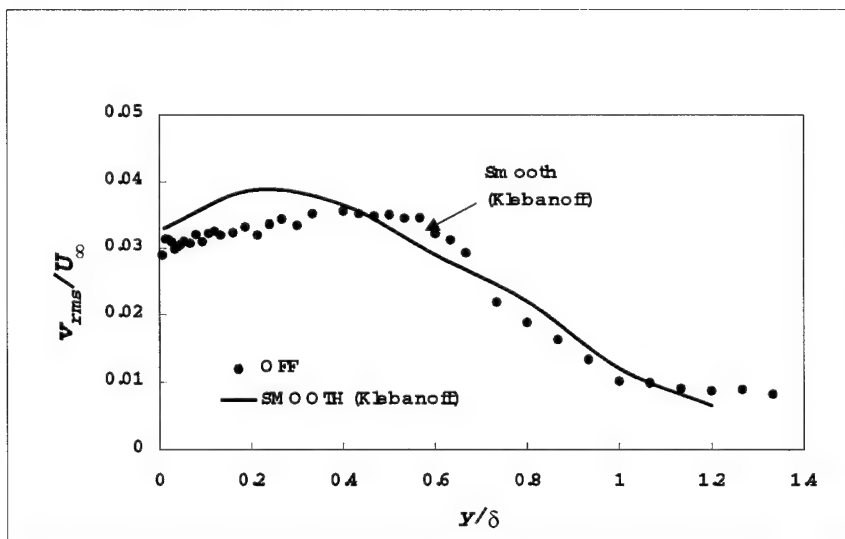
*Figure 22. Laser Doppler Measurements of Baseline Surface-Normal Turbulence Profile at the Downstream End of the Floating Section Compared with Klebanoff's Smooth Wall Profile*

31

The laser Doppler measurements of the effects of the microtiles on the near-wall mean velocity profiles are shown in figures 23 – 25 for the three kinds of pulsed power. A bipolar pulsing caused a marginal reduction in the near-wall region $0.5 < y < 1.5$ mm, and in the region $0.1 < y < 3$ mm for negative unipolar pulsing. There was no effect for a positive unipolar pulsing.

The laser Doppler measurements of the effects of the microtiles on the near-wall surface-normal turbulence intensity profiles are shown in figures 27 – 30 for the three kinds of pulsed power. Here, $T_v\%$ is turbulence intensity in the surface-normal direction, and v_{rms}/V is expressed as a percentage of local surface-normal mean velocity V. There is a marginal reduction in the surface-normal turbulence intensity in the range for bipolar pulsing and in the range for negative unipolar pulsing; there is no effect for positive unipolar pulsing. The mean velocity and surface-normal turbulence intensity measurements suggest that the microtiles cause a weak drag-reducing effect in the near-wall region for bipolar and negative unipolar pulsing; however, these effects are not large enough to be measured clearly by the drag balance.
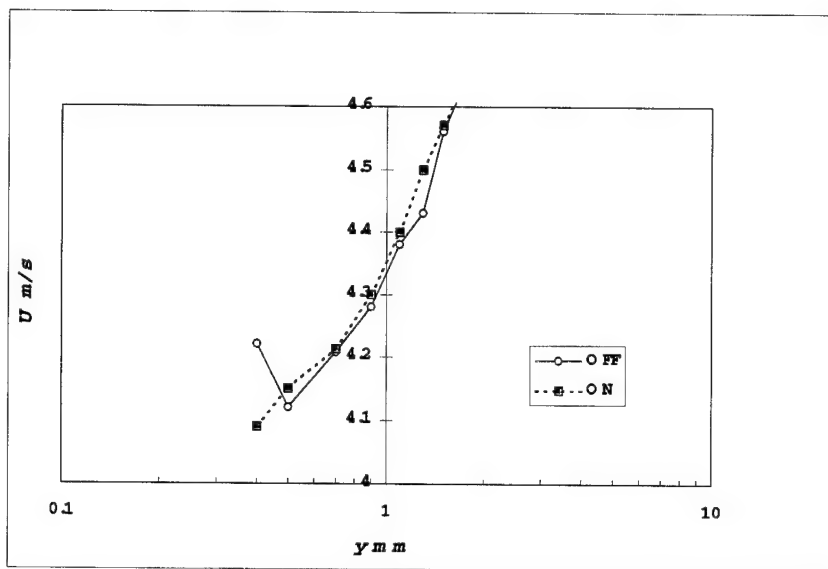
Figure 23. Laser Doppler Measurements of Near-Wall Streamwise Velocity Profile for Bipolar Pulsing, On and Off Conditions (250 Hz, 5.61 m/s, 35.4 mSi/cm, 5 V, 14 A)
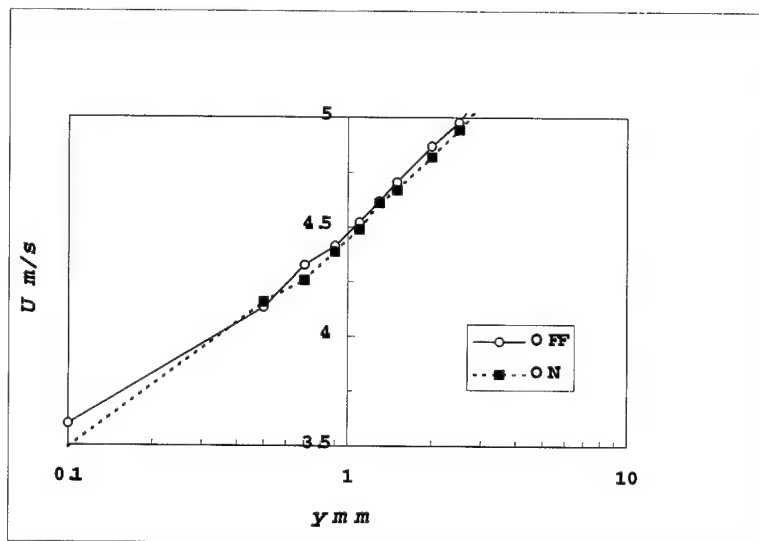
Figure 24. Laser Doppler Measurements of Near-Wall Streamwise Velocity Profile for Negative Unipolar Pulsing, On and Off Conditions (250 Hz, 6.1 m/s, 35.5 mSi/cm, 5.65 – 6 V, 5 A)
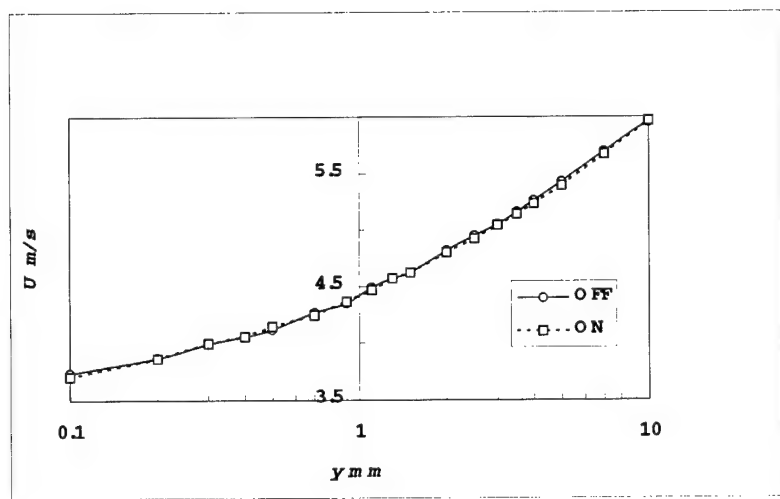
Figure 25. Laser Doppler Measurements of Near-Wall Streamwise Velocity Profile for Positive Unipolar Pulsing, On and Off Conditions (250 Hz, 6.1 m/s, 35.5 mSi/cm, 5.55 – 6 V, 5 A)
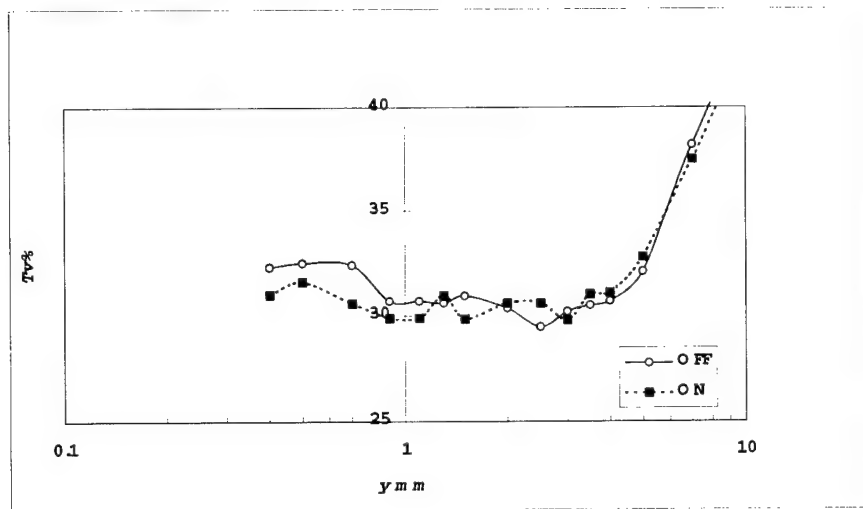

Figure 26. Laser Doppler Measurements of Near-Wall Surface-Normal Turbulence Profile for Bipolar Pulsing, On and Off Conditions (250 Hz, 5.61 m/s, 35.4 mSi/cm, 5 V, 14 A)

34
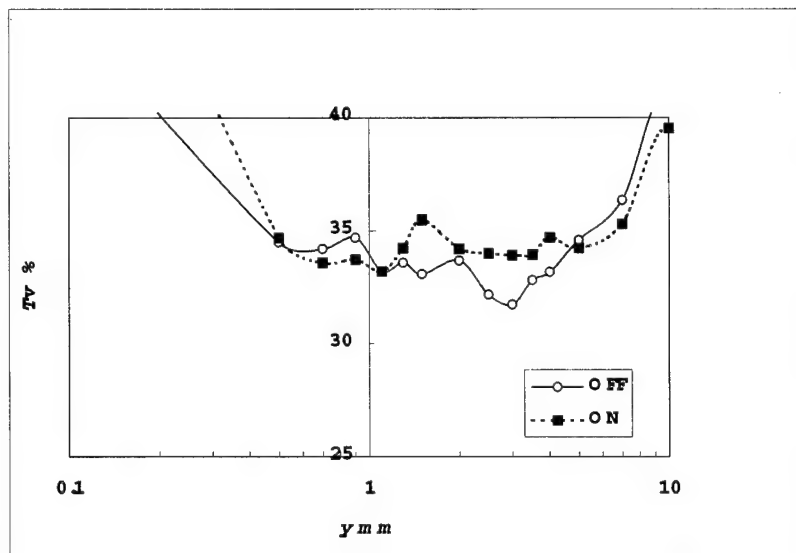
Figure 27. Laser Doppler Measurements of Near-Wall Surface-Normal Turbulence Profile for Negative Unipolar Pulsing, On and Off Conditions (250 Hz, 6.1 m/s, 35.5 mSi/cm, 5.65 – 6 V, 5 A)
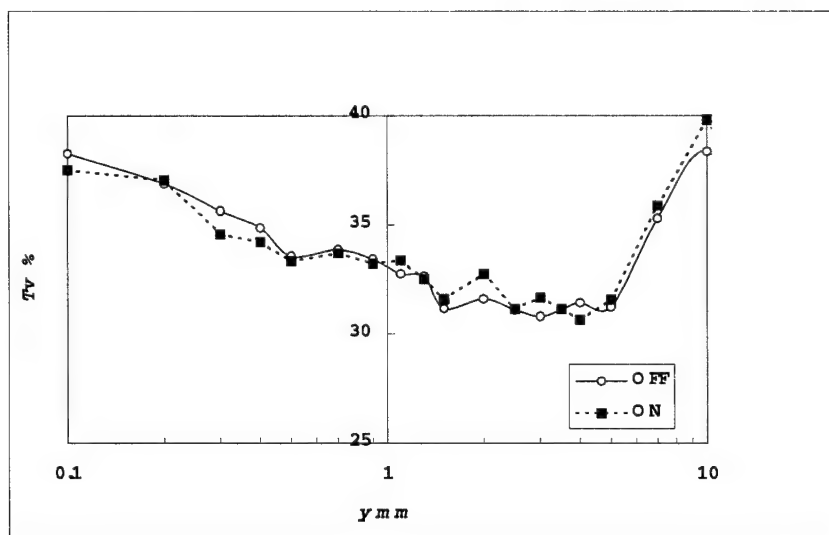

*Figure 28. Laser Doppler Measurements of Near-Wall Surface-Normal Turbulence Profile for Positive Unipolar Pulsing, On and Off Conditions (250 Hz, 6.1 m/s, 35.5 mSi/cm, 5.55 – 6 V, 5 A)*

4.2 MEASUREMENTS OF WALL-PRESSURE FLUCTUATIONS

4.2.1 *Wall-Pressure Fluctuation Sensor*

The sensor consists of an air-filled, end-capped PZT ceramic cylinder with a 2.29-mm outer diameter x 6.35-mm length, potted inside an open metal cylinder with a 3.18-mm inner diameter x 4.8-mm outer diameter x 16-mm length. The sensor is provided with 5.3 m of shielded coaxial cable (2.16-mm outer diameter) and is electrostatically shielded reasonably well. Figure 29 shows a photograph of the sensors mounted on the 78-mm-diameter cylinder model just after the floating cylinder. Two of the sensors are mounted axially behind the microtile center and two are mounted behind the magnets. The probe diameter is about 380 wall units at a flow speed of 5.3 ms.

Table 2 shows the wall-pressure sensor characteristics. The sensitivity (-228 dB//1V/uPa) was measured in an air calibrator at 100 Hz. The sensor should have a flat response from 1 – 10 Hz (depending on preamplifier) to at least 10 kHz. The capacitance difference (860 pF) is the cable capacitance. The 11.0-dB sensitivity difference is due to the cable capacitance (acting as a voltage divider) and to the metal cylinder shielding the ceramic tube wall from the acoustic pressure. The sensitivity loss due to the cable capacitance is 20 log (1500/2360) = 3.9 dB; therefore, the sensitivity loss due to the metal sheath is 11.0 - 3.9 = 7.1 dB. The sheath hole inner diameter is 3.175 mm.

4.2.2 *Computation of Wall-Pressure Spectra*

The sliding window average over frequency is 11 bins wide. The center frequencies of the spectra are separated by 8 Hz, but a Hanning window was used for the fast Fourier transform; therefore, the bandwidth was 1.5*8 = 12 Hz. Before calculating the value of the sliding window average, each bin level had to be converted to a per-Hertz value. To do this, $10\log(12) = 11.8\,dB$ was subtracted from each level. In addition to this, a gain correction of 2.14 dB was added to

each level. Finally, the 11 adjacent bins were averaged and the resulting level was plotted. The original spectrum data were the result of 20 averages. The standard error is

$20\log(1 + \frac{1}{\sqrt{20}}) = 1.7 \text{ dB}$; however, since the frequency bins are also being averaged (N = 31),

the standard error was 1.4 dB. When two of the spectra are averaged, N jumps to 62 and the standard error is 1.0. The real-time spectra from the HP35670 spectrum analyzer and the post-processed spectra from the analog signal compared well.

Figure 29. Photograph of Wall-Pressure Sensors (Cylinder nose is on left. The horizontal ruler shows the alignment of sensor 1 with the middle of the upstream microtile and in between the magnet pairs. The black rectangles are magnets and the vertical shining bands are the electrodes. The knife edge is in the middle of the photograph. Flow is from left to right.)

Table 2. Wall-Pressure Sensor Characteristics

	Sensitivity (dB//1V/uPa)	Capacitance (pF)
Typical raw EDO "microtube"	-217	1500
Present prototype sensor measured at end of 5.3 m cable	-228	2360
Difference	11.0	860

4.2.3   Wall-Pressure Fluctuation Results

The wall-pressure results are shown in figures 30 – 44. The plot variables are defined as follows:

$$\text{RMS PressureInner} = \frac{\sqrt{p'^2}}{\tau_w} \tag{10}$$

$$\text{RMS PressureOuter} = \frac{\sqrt{\overline{p'^2}}}{\left(\frac{1}{2}\rho U_\infty^2\right)} \tag{11}$$

$$\text{Skewness} = \frac{\overline{p'^3}}{\left(\sqrt{\overline{p'^2}}\right)^3} \tag{12}$$

$$\text{Kurtosis} = \frac{\overline{p'^4}}{\left(\sqrt{\overline{p'^2}}\right)^4}. \tag{13}$$

Here, $p_{rms} = \sqrt{p'^2}$, where p' is the instantaneous wall-pressure fluctuation, τ_w is wall-shear stress and $q_0 = \frac{1}{2}\rho U\infty^2$ is the dynamic head. The spectra in inner-layer variables are plotted as $10\log\left(\phi_{p'p'}^{+}\right)$ versus w^+, where $\phi_{p'p'}^{+} = \frac{\phi_{p'p'} U_\tau^2}{\tau_w^2 \upsilon}$, and $w^+ = \frac{(2\pi f)\upsilon}{U_\tau^2}$. Here, p' is the instantaneous wall-pressure fluctuation signal, τ_w is the wall shear stress, ρ is fluid density, U_∞ is freestream velocity, $\phi_{p'p'}$ is the power spectrum of the wall-pressure fluctuation signal, υ is the fluid kinematic viscosity, and ϖ and f are frequencies.

38
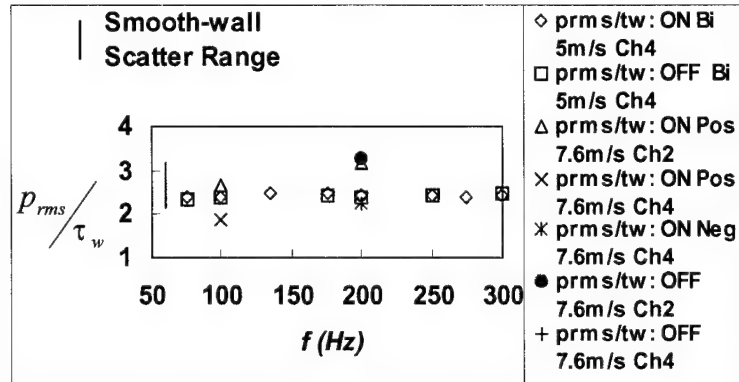
Figure 30. Effect of Pulsing Frequency on Wall-Pressure rms in Wall-Layer Variables
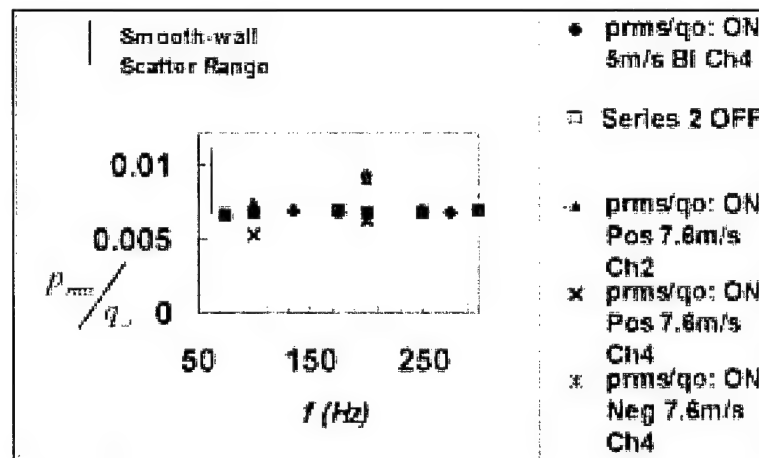

Figure 31. Effect of Pulsing Frequency on Wall-Pressure rms in Outer-Layer Variables
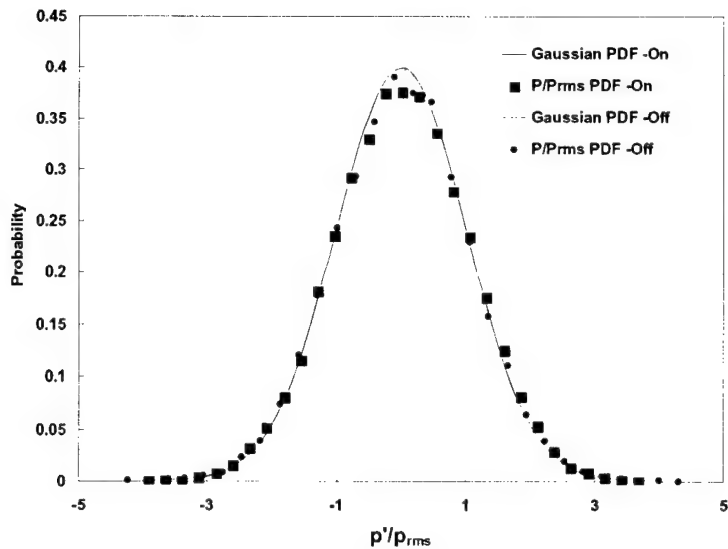
Figure 32. *Comparison of Probability Density Function of On and Off Cases with Gaussian Distribution (Bipolar Pulsing, Sensor #4)*
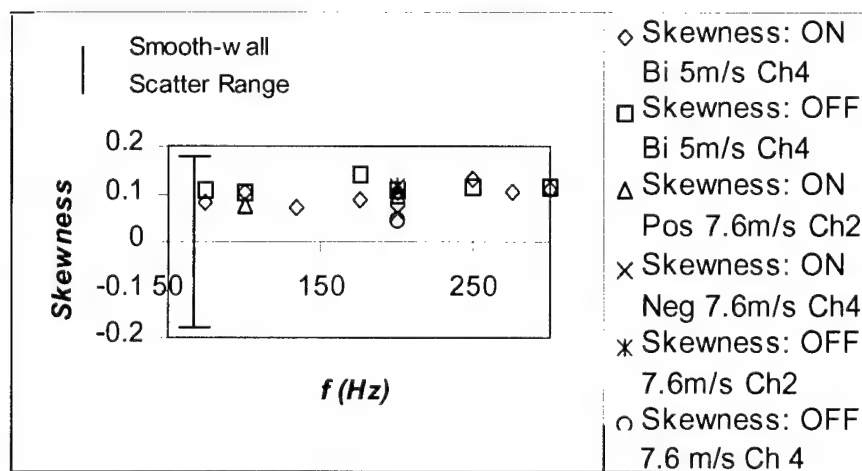
Figure 33a. *Effect of Pulsed Lorenz Force on Skewness of Wall-Pressure Fluctuations (Comparison of On and Off Cases)*
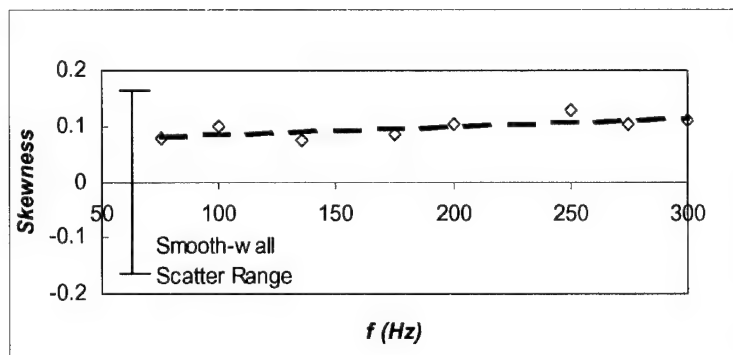
Figure 33b. Effect of Pulsed Lorenz Force on Skewness of Wall-Pressure Fluctuations (Effect of Bipolar Frequency, Sensor #4, Flow Speed 5 m/s) (Broken line indicates mean trend.)
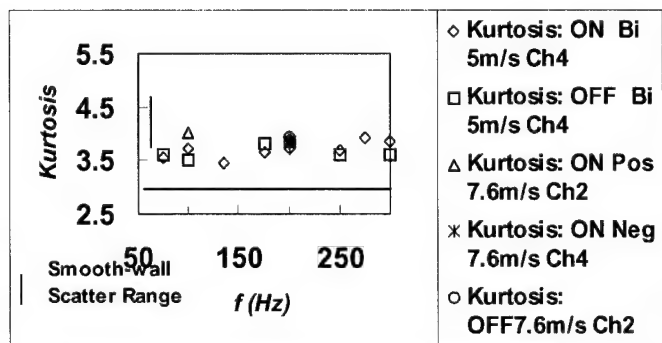
Figure 34a. Effect of Pulsed Lorenz Force on Kurtosis of Wall-Pressure Fluctuations (Comparison of On and Off Cases)
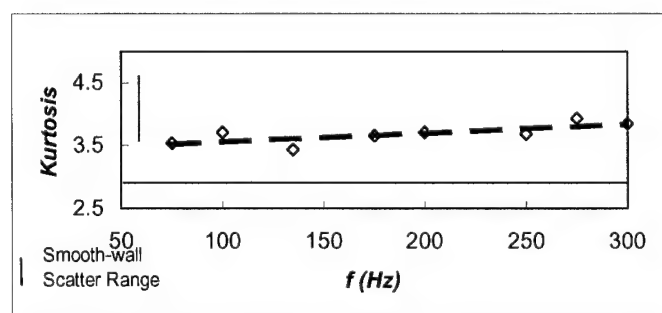
Figure 34b. Effect of Pulsed Lorenz Force on Kurtosis of Wall-Pressure Fluctuations (Effect of Bipolar Pulsing Frequency, Sensor #4, Flow Speed 5 m/s) (Broken line indicates mean trend.)

41
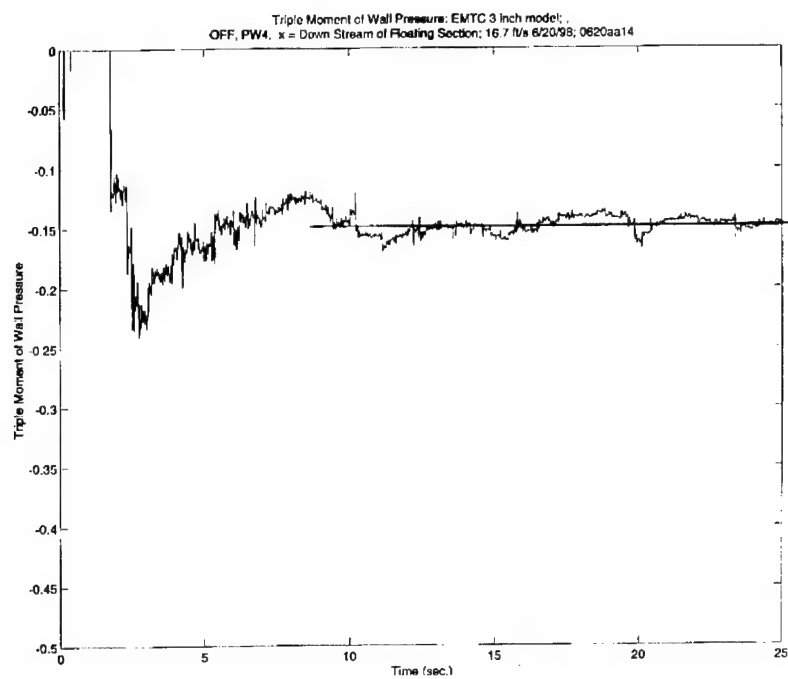
Figure 35. Skewness of Wall Pressure Fluctuations at Station 4 (Pulsing Off)
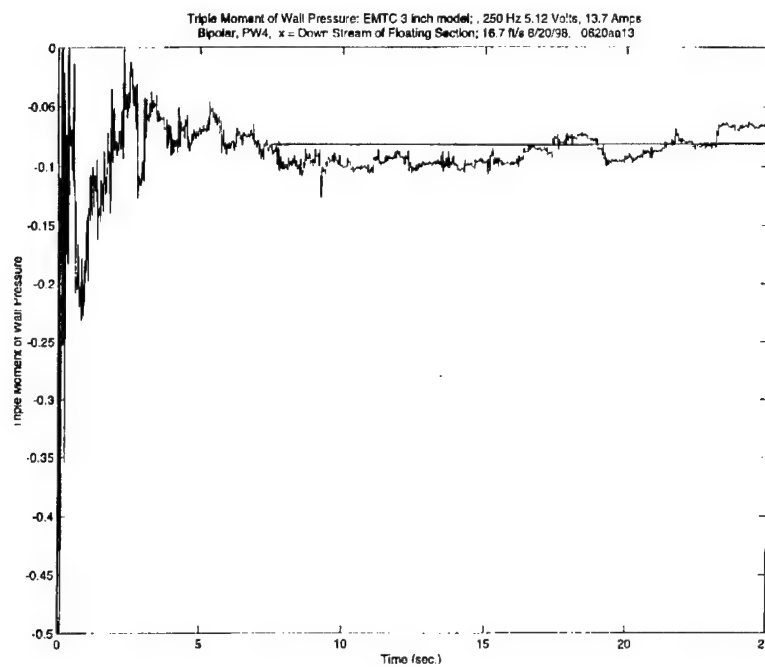
Figure 36. Skewness of Wall Pressure Fluctuations at Station 4 (Bipolar Pulsing at 250 Hz)

42
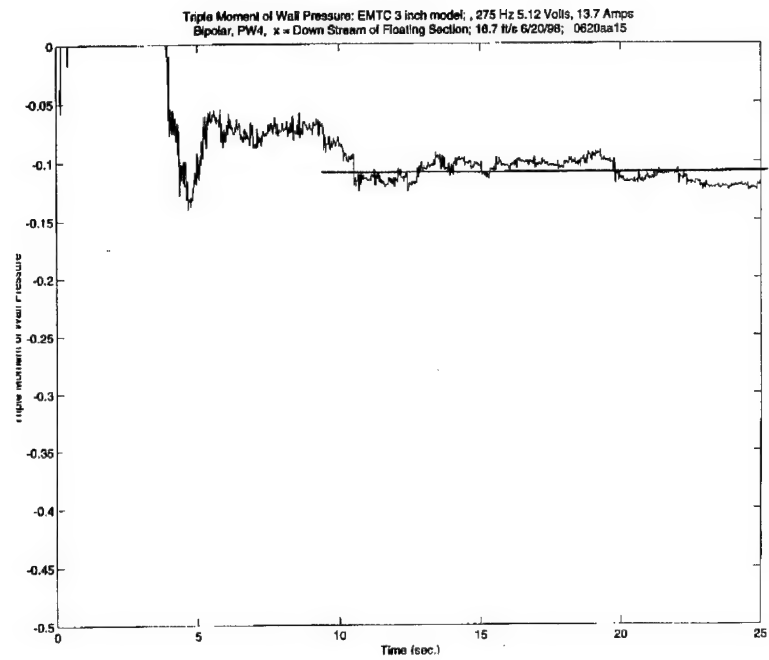
**Figure 37. Skewness of Wall Pressure Fluctuations at Station 4
(Bipolar Pulsing at 275 Hz)**
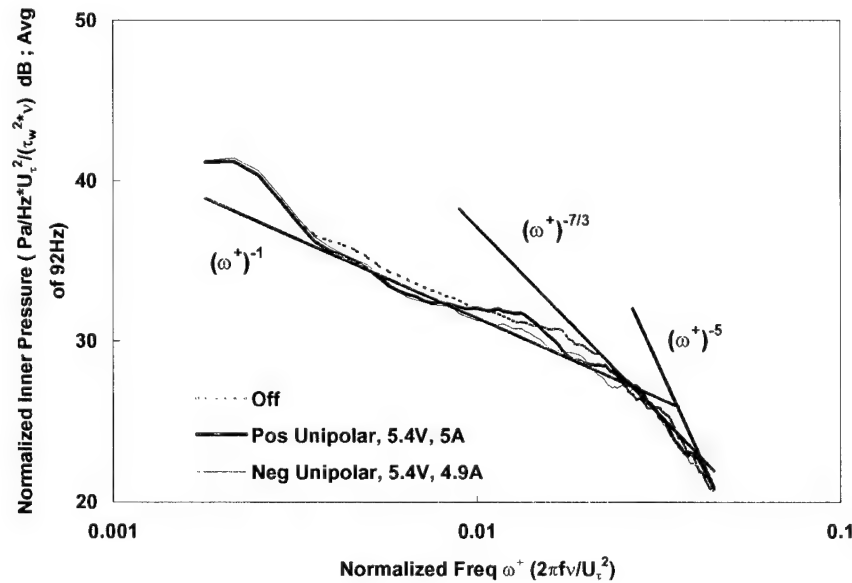
**Figure 38. Inner-Layer Plot Comparison of Wall Pressure Spectra (Power: Positive and
Negative Unipolar, Wall Pressure #4, Pulsing Frequency 100 Hz)
(Solid lines for comparison are -1, -2 1/3, and -5 frequency power laws.)**

43
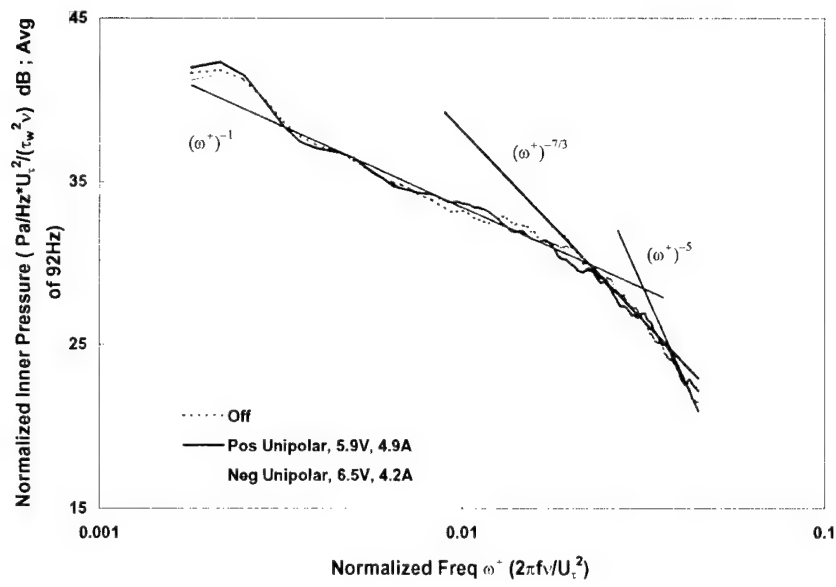
Figure 39. Inner-Layer Plot Comparison of Wall-Pressure Spectra (Power: Positive and Negative Unipolar, Wall Pressure #4, Pulsing Frequency 200 Hz) (Solid lines for comparison are -1, -2 1/3, and -5 frequency power laws.)
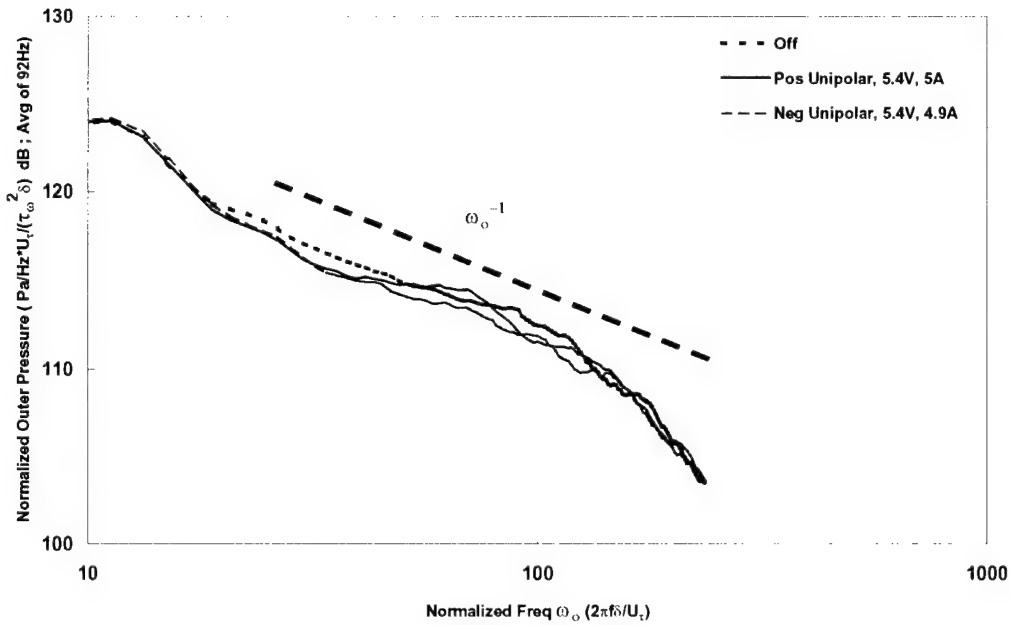
Figure 40. Wall-Pressure Spectra in Outer Layer Variables Showing the Effects of Unipolar Pulsing of Lorenz Power (Pulsing Frequency 100 Hz, Sensor #4, Flow Speed 7.56 m/s)

44
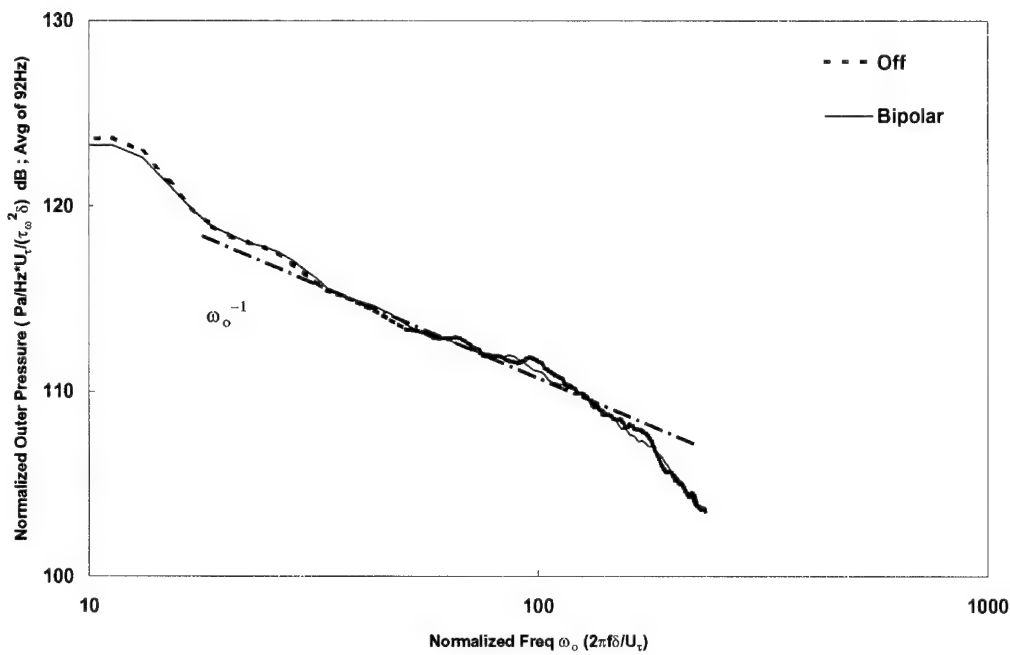
Figure 41. Wall-Pressure Spectra in Outer-Layer Variables Showing the Effects of Bipolar Pulsing of Lorenz Power (Pulsing Frequency 100 Hz, 5.725 V, 13.95 A, Sensor #4, Flow Speed 7.56 m/s)
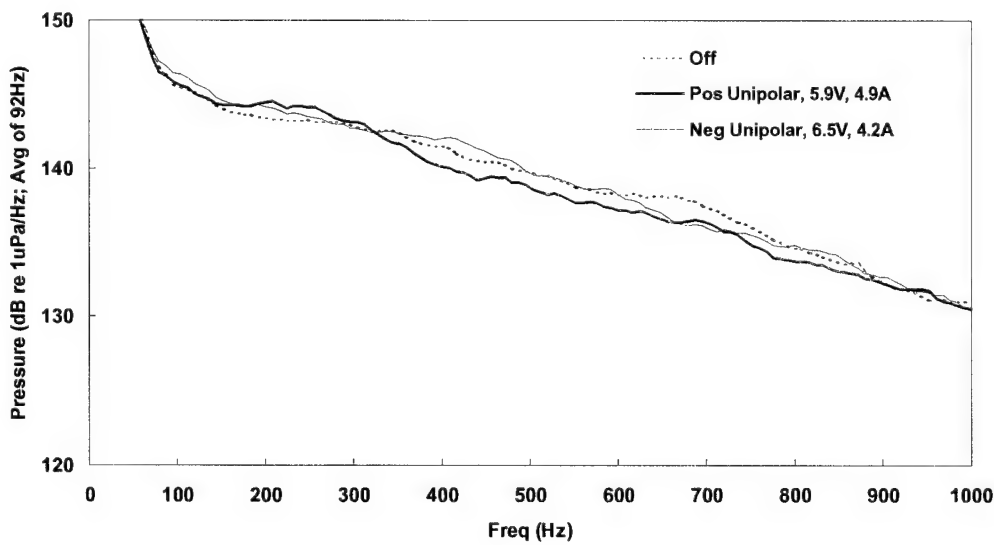
Figure 42. Wall-Pressure Spectra Comparing Baseline with Effect of Unipolar Pulsing of Lorenz Power (Pulsing Frequency 200 Hz, Sensor #2, Flow Speed 7.56 m/s)

45
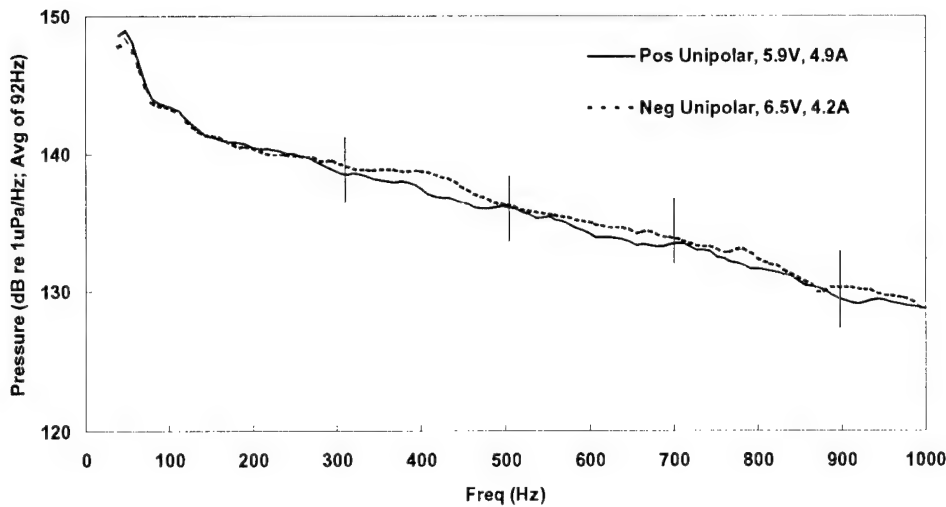
Figure 43. Wall-Pressure Spectra Showing the Relative Effect of Unipolar Pulsing of Lorenz Power (Pulsing Frequency 200 Hz, Flow Speed 7.56 m/s) (Vertical bars are spaced 200 Hz apart. Power: positive unipolar (5.9 V and 4.9 A) and negative unipolar (6.5 V, 4.2 A), Sensor #4)
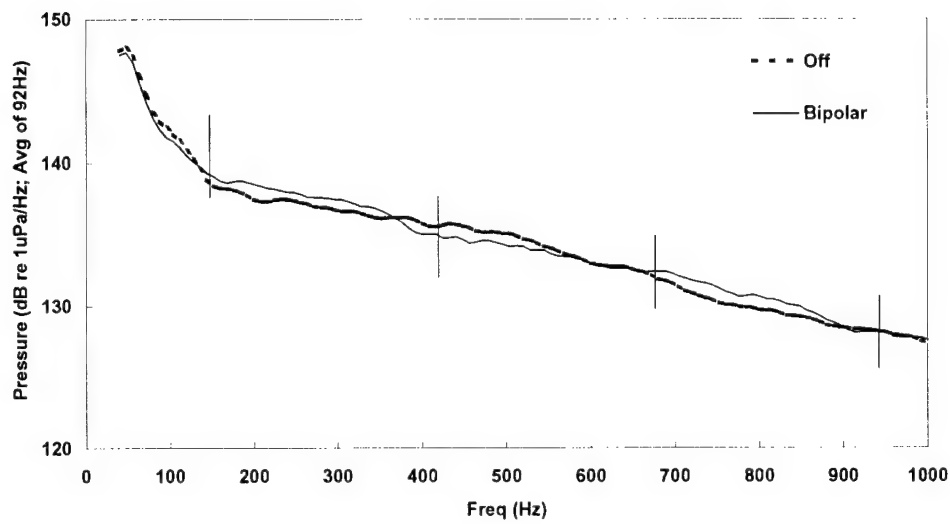
Figure 44. Wall-Pressure Spectra Showing the Relative Effect of Bipolar Pulsing of Lorenz Power (Pulsing Frequency 275 Hz, Flow Speed 7.56 m/s) (Vertical bars are spaced 275 Hz apart. Power: bipolar 5.25 V, 13.8 A, Sensor #4)

46

4.2.4   Root-Mean-Square of Pressure Fluctuations

The rms values of wall-pressure and wall-shear fluctuations tend to be linearly related. In this sense, wall-pressure data can be doubly valuable. The rms values of the wall-pressure fluctuations for Lorenz force on-and-off cases for various pulsing frequencies are shown in figure 29 in inner layer scales, and in figure 30 in outer-layer scales. The figures include the scatter range of published data in smooth walls. The present data are generally in the lower ranges of the scatter band. Sensor 4 indicates some reduction at 100 Hz for positive unipolar pulsing.

4.2.5   Skewness and Kurtosis

The probability density function of the wall-pressure fluctuation signal for the on and off cases are compared with the Gaussian distribution in figure 31. The closeness to the Gaussian distribution indicates that skewness and kurtosis should be close to 0 and 3, respectively. The effect of pulsing frequency f (not to be confused with frequency f of spectra) on the skewness and kurtosis of the wall-pressure signal are shown in figures 32 and 33, respectively. The smooth-wall scatter ranges are included. The kurtosis is closer to the Gaussian value than those reported for smooth walls. Figures 32a and 33b show that, at station 4, bipolar pulsing leads to a gradual increase in both skewness and kurtosis with frequency of pulsing. Because skewness retains the sign of the original signal, increasing skewness with frequency of pulsing indicates the increasing appearance of positive spikes in the wall-pressure fluctuation signal. At and below 200 Hz of pulsing, the skewness tends to be slightly lower than the baseline off case (figure 32a). The effect of pulsing on the stationary levels of the triple moment of the wall-pressure fluctuation signal is compared in figures 34 – 36. The off case level is -0.15, while it increases to 0.075 at 250 Hz and 0.1 at 275 Hz of bipolar pulsing.

4.2.6 Wall-Pressure Spectra

The effect of pulsing on wall-pressure spectra is shown in figures 37 and 38 in inner-layer variables for 100 and 200 Hz of unipolar pulsing. The spectra are compared with three frequency power laws, whose exponents are -1, -2 1/3, and -5. The Reynolds number Re_0 is about 3300, and the -1 power law is observed for nearly a decade of frequency. The outer-layer scale plot in figure 39 also shows that this region has the same power law. Bradshaw[23] and Panton and Lineberger[24] have pointed out that the sources of wall-pressure fluctuations for this region are in the logarithmic layer, which is an overlapping region of inner and outer layers. Now, the effect of unipolar and bipolar pulsing is compared in the spectra in figures 39 and 40, respectively, where the baseline off case is included. The bipolar pulsing case matches the off case closely, and therefore has no effect on the logarithmic layer sources. On the other hand, the unipolar pulsing cases deviate around the off case by a few decibels. Thus, it is concluded that the microtiles are affecting the wall-pressure fluctuation sources in the logarithmic region during unipolar pulsing. The wall-pressure spectra (not non-dimensionalized) for unipolar pulsing at 200 Hz is shown in figure 41. It can be seen that there is a sustained reduction of wall-pressure fluctuations of a few decibels in the frequency range of 300 to 900 Hz due to positive unipolar pulsing. Figure 38 shows that this sustained reduction is not present at a pulsing frequency of 200 Hz, and the closer clustering to the mean trend in the -1 power-law region is reminiscent of the bipolar pulsing case mentioned earlier in reference to figure 40; thus, pulse shape and frequency of pulsing of the microtile power does affect the turbulence in the logarithmic region.

There is also a smaller but clear region of -2 1/3 power law in figures 37 and 38. This may be compared with the results of Gravante et al.[25] Olivero-Bally et al.[26] have shown that this region is fed by sources in the upper part of the buffer layer. Figure 38 shows that this power law is obeyed by the off case at a lower frequency, followed by the positive and then the negative unipolar case. Based on the results in figures 37 – 41, the microtiles alter the turbulence in the logarithmic as well as in the upper parts of the buffer layer.

It is interesting that the small microtiles (figure 8) are affecting the sources of wall-pressure fluctuations residing in the logarithmic region of the turbulent boundary layer, which are beyond the depth of where the Lorenz force is applied (figures 2 and 4). Some additional manifestations of this are considered in figures 42 and 43.

Figures 42 and 43 compare the effects of Lorenz force pulsing on the wall-pressure spectra in the frequency range where the sources are attributable to the logarithmic region of the turbulent boundary layer. In figure 42, the effects of positive and negative unipolar pulsing at 200 Hz are compared. In figure 43, the effects of bipolar pulsing at 275 Hz are compared with the off case. Both figures contain vertical bars delineating frequency bands equal to the pulsing frequency. Generally, near the middle of the frequency regions of the vertical marks, the differences in power between the spectra amplify, while they diminish at the band marks. The power amplification takes place at frequencies Nf_p and diminish at $Nf_p \pm {f_p}/{2}$, where f_p is the pulsing-frequency and N are integers 2, 3, and 4 in figure 43 and 1, 2, and 3, in figure 44. Note that the pulsing frequencies Nf_p are in the range of resonance of the wall-layer-based mechanism of the microtiles described in section 2.2.1 and 2.3. The pattern in figures 42 and 43 may be interpreted to mean that, between the two cases being compared, the pulsed microtiles cause a relative stretching of vortices in the log layer at frequencies Nf_p and a compression at $Nf_p \pm {f_p}/{2}$. The conclusion is that pulsing does indeed lead to resonance, although the degree achieved here is weak.

5. CONCLUSIONS

A wall-layer based electromagnetic microtile arrangement has been developed for turbulence control. The flow mechanism over a single microtile has been investigated via modeling, DNS simulation, and channel flow visualization experiments. The following conclusions can be drawn:

- The pulsed power microtiles may be viewed as actuators for aggregating "pillows" of vorticity above them. Such a pillow consists of a ring vortex, with a streamwise pair of vorticity whose rotation is opposite to that of naturally occurring, near-wall vortex pairs in the near-wall region of a turbulent boundary layer.

- The physical relevance of smooth-wall-based simulation and modeling of the mechanism to experiments can become complicated unless care is taken to minimize the roughening of the surface due to rust deposition and corrosion.

- A method of measuring the surface area and time-integrated drag in an axisymmetric body in an electrically charged salt water medium has been developed.

- A clear surface area and time-integrated viscous drag reduction within the parameter ranges of Lorenz force of the present experiment have not been observed.

- Scaling arguments indicate that while the length and time scales imposed by the actuator appear to be correct, the amplitude of salt water fluid pumping is currently inadequate.

- The mean velocity and surface-normal turbulence intensity measurements suggest that the microtiles cause a weak drag reducing effect in the near-wall region for bipolar and negative unipolar pulsing. However, these effects are not large enough to be measured clearly by the drag balance.

- In certain parameter ranges, the microtiles can marginally lower the skewness of the wall-pressure signal. Bipolar pulsing causes a slight increase in skewness and kurtosis of the wall-pressure fluctuation signal with pulsing frequency.

- In certain parameter ranges, the microtiles can lower the wall-pressure spectrum marginally. Effects of pulsing of power to the microtiles have been observed on the sources of wall-pressure fluctuations residing in the logarithmic region of the boundary layer. Although weak, this pulsing leads to an amplification of wall-pressure spectrum power that provides support to the wall-layer resonance mechanism of the proposed microtiles.

6. REFERENCES

1. W. Ritchie, "Experimental Researches in Voltaic and Electromagnetism," *Philosophical Transactions of the Royal Society (London)*, vol. 122, 1832, pp. 279 – 298.

2. N. Nosenchuck and G. L. Brown, "Discrete Spatial Control of Wall Shear Stress in a Turbulent Boundary Layer," in *Near-Wall Turbulent Flows*, Elsevir, 1993, pp. 689 – 698.

3. J. C. S Meng, S. A. Huyer, J. M. Castano, D. P. Thivierge, and P. J. Hendricks, "Experimental Study of the Spanwise Vortex Resonance Hypothesis for Turbulent Drag Reduction Over a Flat Plate in Salt Water," NUWC-NPT Technical Report 10,680, Naval Undersea Warfare Center Division Newport, RI, 1997.

4. Y. Du and G. E. Karniadakis, "Suppressing Wall-Turbulence via a Transverse Travelling Wave," *Science*, vol. 288, 2000, pp. 1230 – 1234.

5. X. Fan and G. L. Brown, "Experiments on the Electromagnetic Control of Turbulence," Paper No. AIAA 97-2123, *American Institute of Aeronautics and Astronautics*, Washington, DC, 1997.

6. C. Henoch and J. Stace, "Experimental Investigation of a Salt Water Turbulent Boundary Layer Modified by an Applied Streamwise Magnetohydrodynamic Body Force," *Physics of Fluids*, vol. 7, no. 6, 1995, pp. 1371 – 1383.

7. P. R. Bandyopadhyay and J. M. Castano, "Micro-Tiles for Electromagnetic Turbulence Control in Salt Water - Preliminary Investigations," *Symposium on Turbulence Modification and Drag Reduction*, ASME Summer Meeting, San Diego, CA, FED, vol. 237, vol. 2, July 7 – 11 1996, pp. 53 – 60.

8. S. Wilkinson and B. S. Lazos, "Direct Drag and Hot-Wire Measurements on Thin-Element Riblet Arrays," *IUTAM Symposium on Turbulence Management and Relaminarization*, Bangalore, India, Jan. 19 – 23 1987.

9. C. Crawford and G. Karniadakis, "Shear-Stress Modification and Vorticity Dynamics in Near-Wall Turbulence," *Journal of Fluid Mechanics* (due to appear).

10. T. W. Berger, J. Kim, C. Lee, and J. Lim, "Turbulent Boundary Layer Control Utilizing the Lorenz Force," *Physics of Fluids*, vol. 12, no. 3, 2000, pp. 631 – 649.

11. P. R Bandyopadhyay and R. Balasubramanian, "Structural Modeling of the Wall Effects of Lorenz Force," *ASME Journal of Fluids Engineering*, vol. 118, 1996, pp. 412 – 414.

12. Private communication with L. Kral, McDonnell Douglas, St. Louis, MO, 1998.

13. S. N. Singh and P. R. Bandyopadhyay, "Linear Feedback Control of Boundary Layer Using Electromagnetic Microtiles," *ASME Journal of Fluids Engineering*, vol. 119, 1997, pp. 852 – 858.

14. W. J. Jueng, N. Mangiavacchi, and R Akhavan, "Suppression of Turbulence in Wall-bounded Flows by High Frequency Spanwise Oscillations," *Physics of Fluids*, vol. A4, no. 8, 1992, pp. 1605 – 1607.

15. P. R. Bandyopadhyay, "Review of Self-Sustaining Mechanism of Wall Turbulence," *AIAA Journal*, vol. 36, 1998, pp. 1549 – 1552.

16. F. Hatay, P. L. O' Sullivan, S. Biringen, and P. R. Bandyopadhyay, "Numerical Simulation of Secondary Flows in Channels Driven by Applied Lorenz Forces," *AIAA Journal of Thermophysics and Heat Transfer*, vol. 11, no. 3, 1997, pp. 446 – 453.

17. J. C. S. Meng, "Engineering Insight of Near-Wall Microturbulence for Drag Reduction and Derivation of a Design Map for Seawater Electromagnetic Turbulence Control," *Proceedings of the International Symposium on Seawater Drag Reduction*, pp. 359 – 367, Newport, RI, July 22 – 23, 1998.

18. H. Schlichting, *Forced Transition Boundary Layer Theory*, McGraw Hill, New York, 1978

19. J. M. Castano, "Microbubble Drag Reduction on a Submerged Axisymmetric Body," M.S. Thesis, Penn State University, 1985.

20. P. L. O'Sullivan and S. H. Biringen, "Direct Simulations of Low Reynolds Number Turbulent Channel Flow with EMHD Control," *Physics of Fluids*, vol. 10, no. 5, 1998, p. 1169.

21. K. Choi, J. DeBisschop, and B. R. Clayton, "Turbulent Boundary-Layer Control by Means of Spanwise-Wall Oscillation," *AIAA Journal*, vol. 36, 1998, pp. 1157 – 1163.

22. P. R. Bandyopadhyay, "Stokes' Mechanism of Drag Reduction," NUWC-NPT Technical Report 11,316, Naval Undersea Warfare Center Division, Newport, RI, 15 October 2001.

23. P. Bradshaw, "Inactive Motion and Pressure Fluctuations in Turbulent Boundary Layers," *Journal of Fluid Mechanics*, vol. 30, no. 2, 1967, pp. 241 – 258.

24. R. L. Panton and J. H. Lineberger, "Wall-Pressure Spectra Calculations for Equilibrium Boundary Layers," *Journal of Fluid Mechanics*, vol. 65, no. 2, 1974, pp. 261 – 287.

25. S. P. Gravante, C. E. Naguib, C. E. Wark, and H. M. Nagib, "Characterization of the Pressure Fluctuations Under a Fully Developed Turbulent Boundary Layer," *AIAA Journal*, vol. 36, no. 10, 1998, pp. 1808 – 1816.

26. P. Olivero-Bally, B. E. Foresterier, E. Focquenoy, and P. Olivero, "Wall-Pressure Fluctuations in Natural and Manipulated Turbulent Boundary Layers in Air and Water," *American Society of Mechanical Engineers Winter Annual Meeting*, New Orleans, LA, 1993.

INITIAL DISTRIBUTION LIST

Addressee	No. of Copies
Naval Surface Warfare Center/Carderock Division (J. Fein, M. Donnelly, T. Farabee)	3
Office of Naval Research (ONR-333 -- P. Purtell, K. Ng, T. McMullen, S. Lekoudis, W. S. Vaughan)	5
Naval Research Laboratory (W. Sandberg, R. Ramamurti)	2
Naval Undersea Warfare Center Division Keyport (J. Meng)	1
Defense Advanced Research Projects Agency (R. Wlezian)	1
University of California/San Diego (J. Kim)	1
Princeton University (A. Smits, G. L. Brown)	2
Yale University (K. R. Sreenivasan)	1
Brown University (G. Karniadakis, K. Breuer)	2
Virginia Polytechnical Institute (D. P. Telionis, R. L. Simpson)	2
University of Illinois (R. Adrian, R. Balasubramanian, J. Craig Dutton)	3
University of Colorado at Boulder (S. Biringen)	1
Stanford University (B. Cantwell, P. Bradshaw)	2
University of Houston (F. Hussain)	1
University of Michigan (G. M. Faeth)	1
NASA Langley Research Center (J. B. Anders)	1
PSU ARL (R. L. Simpson, M. Billet, S. Deutch)	3
Massachusetts Institute of Technology (M. Triantafyllou, P. S. Virk)	2
University of Texas/Austin (R. Panton, D. Bogard)	2
University of Southern California (R. Blackwelder)	1
Defense Technical Information Center	2
Center for Naval Analyses	1